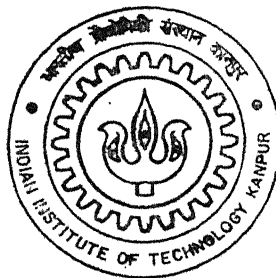


7110504

# **APPLICATION OF RAY TRACING IN TOMOGRAPHIC RECONSTRUCTION OF DEFECTS IN ORTHOTROPIC MATERIALS**

**By**

**Ashish Kumar Sharma**



TH  
ME/2003/M  
Sh 23 a

**DEPARTMENT OF MECHANICAL ENGINEERING**

**Indian Institute of Technology Kanpur**

**FEBRUARY, 2003**

# APPLICATION OF RAY TRACING IN TOMOGRAPHIC RECONSTRUCTION OF DEFECTS IN ORTHOTROPIC MATERIALS

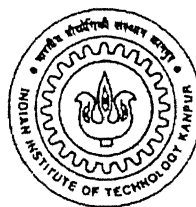
A Thesis Submitted  
in Partial Fulfillment of the Requirements  
for the Degree of

**MASTER OF TECHNOLOGY**

February, 2003

*by*

**ASHISH KUMAR SHARMA**



DEPARTMENT OF MECHANICAL ENGINEERING  
INDIAN INSTITUTE OF TECHNOLOGY  
KANPUR – 208016 (INDIA)

30 MAY 2003

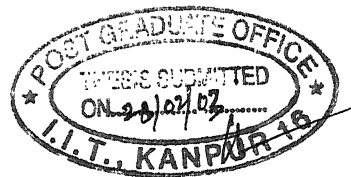
पुरुषोत्तम काशीनाथ केनकर पुस्तकालय  
भारतीय बौद्धिकी संस्थान कानपुर

अवधि क्र० A.....143463.....



7143463

# CERTIFICATE



It is certified that the work contained in the thesis entitled “**Application of Ray Tracing in Tomographic Reconstruction of Defects in Orthotropic Materials.**” by *Ashish Kumar Sharma* has been carried out under my supervision and that this work has not been submitted elsewhere for a degree.

Dr V Raghuram,  
(Sr Research Engineer)  
Department of Mechanical Engg.  
Indian Institute of Technology, Kanpur

Dr N N Kishore  
(Professor and Head)  
Department of Mechanical Engg.  
Indian Institute of Technology, Kanpur



## ACKNOWLEDGEMENTS

I wish to express my deep sense of gratitude to my ever-cherished guides Dr. N.N. Kishore and Dr. V. Raghuram for their guidance, invaluable suggestions and constant encouragement. I am sincerely thankful for their valuable suggestions in my academic as well as personal life.

I am paying my great regards to Dr. Bishakh Bhattacharya and Dr. P.M. Dixit for giving me invaluable exposure to composite materials and numerical techniques respectively.

I wish to express my special thanks to Mr. S. K. Rathore for his invaluable suggestions and constant encouragement towards completion of my work.

I appreciate and extend my thanks to my lab mates Mr. Mukul Shukla, Bhanu, Ramakrishna, Samuel and Dattatraya for their suggestions while I was developing the code.

I would like to thank all my friends IIT friends Santosh, Pavan, Ravindra, Debadi, Manish and Abhishek for making my stay at IITK very enjoyable and memorable. I will cherish the moments forever.

I wish to express my heartfelt thanks to my brothers Amit and Aditya for their endless love and care.

Finally, I am grateful to the Almighty and my parents for what I am today.

Indian Institute of Technology, Kanpur.  
February, 2003

-Ashish Kumar Sharma

## Abstract

New technological needs are leading to the development of new materials with enhanced mechanical properties for specific applications. The knowledge of the elastic properties of these new materials, i.e. the elastic constants, is in practice of great importance. Many of these new materials are ceramics and composites. Conventional methods are not very much successful for determining these material properties.

The laser ultrasonic technique, which uses lasers to generate and detect ultrasound at a distance, without any contact to the specimen, are more popular and successful for such materials. If the samples can be cut in predetermined directions, elastic constants can be determined from velocity data in these directions with the number of measurements equal to number of unknown independent elastic constants. Choosing an appropriate propagation direction can maximize the accuracy of the elastic constant measurement. The process of image reconstruction using velocity data is termed as tomography.

In the present work, a tomographic image reconstruction model is developed using ray tracing. The method reconstructs a two dimensional object, with internal defects, in terms of independent parameters, like elastic constants of the material. Single mode measurement time of flight data is used for the reconstruction. The proposed model is a two stage process, which involves conventional ART algorithm corrections in the first stage and solution of a set of nonlinear equations in the second stage. For defects like circle and ellipse, edge detection is taken into consideration, during ray tracing. The method is found to perform well for rectangular, as well as curved defects.

*Dedicated to*

**MY PARENTS**

*Who sacrificed their dreams*

*So that mine could come true*

# CONTENTS

<b>CERTIFICATE</b>	<b>ii</b>
<b>ACKNOWLEDGEMENTS</b>	<b>iv</b>
<b>ABSTRACT</b>	<b>v</b>
<b>LIST OF FIGURES</b>	<b>viii</b>
<b>CHAPTER 1      INTRODUCTION</b>	<b>1</b>
1.1      Introduction	1
1.2      Literature Survey	2
1.3      Present Work	4
1.4      Thesis Organization	6
<b>CHAPTER 2      BASICS OF ULTRASONIC WAVE PROPAGATION                     IN ANISOTROPIC MATERIALS</b>	<b>6</b>
2.1      Introduction	6
2.2      Equation of motion	7
2.3      Plane wave propagation in bulk materials	8
2.4      Phase and Group Velocity	11
2.5      Relation between the phase and group velocities	13
2.6      Slowness surface	14
2.7      Fundamentals of Reflection and Refraction	17
2.8      Snell's law	19
2.9      Closure	22
<b>CHAPTER 3      RAY TRACING</b>	<b>23</b>
3.1      Introduction	23
3.2      Theory	24
3.3      Ray Tracing Algorithm	28
3.4      Edge correction	29
3.5      Closure	30
<b>CHAPTER 4      TOMOGRAPHY</b>	<b>31</b>
4.1      Introduction	31
4.2      Conventional ART Algorithm	31
4.3      MART algorithms	33
4.4      Tomography as applied to composite materials	35
4.5      Flow diagram for tomographic image reconstruction program	37
4.6      Closure	38

<b>CHAPTER 5</b>	<b>RESULTS AND DISCUSSIONS</b>	<b>39</b>
5.1	Reconstruction using simulated data	39
5.1.1	Rectangular defect	39
5.1.2	Elliptical defect	44
5.2	Reconstruction using experimental data	51
5.3	Effect of various parameters on the performance of the Algorithm	53
5.4	Closure	56
 <b>CHAPTER 6</b>	 <b>CONCLUSIONS</b>	 <b>57</b>
6.1	Conclusions	57
6.2	Scope for future work	57
REFERENCES		<b>58</b>
APPENDIX-A		<b>60</b>
APPENDIX-B		<b>63</b>

# LIST OF FIGURES

2.1	Wavefront moving in rectangular coordinate system	9
2.2	Deviation between phase direction and ray direction	12
2.3	Relation between phase velocity vector group velocity vector	14
2.4	A general slowness diagram for an anisotropic material	16
2.5	Representation of reflected/transmitted wave modes using slowness diagram	17
2.6	Different type of acoustic wave interaction with material discontinuities	18
2.7	Acoustic wave incident on an interface between two anisotropic media	19
2.8	Generalized Snell's law for arbitrarily anisotropic media	22
3.1	An example showing different iterations in a two point ray tracing method	23
3.2	Fiber orientation, phase velocity and group velocity direction relative to cartesian coordinate system	25
3.3	Edge detection	29
3.4	Detection of interface boundary	30
4.1	Weight function $w_{ij}$ for $i^{\text{th}}$ ray and $j^{\text{th}}$ pixel	32
5.1	Ray paths for group velocity angle 16.7 degree	40
5.2	Ray paths for group velocity angle $73.3^\circ$	41
5.3	Reconstruction based on $C_{11}$ for rectangular defect	42
5.4	Reconstruction based on $C_{33}$ for rectangular defect	42
5.5	Reconstructed based on density for rectangular defect	43
5.6	Variation of average error with iteration	43
5.7	Specimen with elliptical defect	45
5.8	Ray path for group velocity angle $73.3^\circ$	45
5.9	Reconstruction based on $C_{11}$ for elliptical defect	46
5.10	Reconstruction based on $C_{33}$ for elliptical defect	46
5.11	Reconstruction based on density for elliptical defect	47
5.12(a)	Reconstruction based on $C_{11}$ after 1 <sup>st</sup> iteration for elliptical defect	47
5.12(b)	Reconstruction based on $C_{11}$ after 2 <sup>nd</sup> iteration for elliptical defect	48
5.12(c)	Reconstruction based on $C_{11}$ after 3 <sup>rd</sup> iteration for elliptical defect	48
5.12(d)	Reconstruction based on $C_{11}$ after 4 <sup>th</sup> iteration for elliptical defect	49
5.12(e)	Reconstruction based on $C_{11}$ after 5 <sup>th</sup> iteration for elliptical defect	49

5.12(f)	Reconstruction based on $C_{11}$ after 6 <sup>th</sup> iteration for elliptical defect	50
5.13	Variation of average error with iteration	50
5.14	Specimen with square defect	52
5.15	Image reconstruction for $C_{11}$ using experimental data	52
5.16	Average error vs. relaxation parameter	54
5.17	Effect of Number of projections through a pixel on performance of the algorithm	54
5.18	Reconstructed image for $C_{33}$ without applying edge detection	55
5.19	Reconstructed image for $C_{33}$ after applying edge detection	56
B-1	Experimental setup	61
B-2	Photograph of LBU setup	62

# Chapter 1

## Introduction

### 1.1 INTRODUCTION

The search for ever lighter, stiffer, and tougher materials from which to construct aerospace vehicles has led inexorably towards more highly engineered, lower density materials like composite materials. The novelty and expense of composite materials has meant, historically, that they are thoroughly inspected prior to use, typically using ultrasonic non-destructive testing.

Ultrasonic materials characterization is the most important application of ultrasonics in aerospace engineering and engineering mechanics. Historically, ultrasonic nondestructive testing (NDT) has been used almost exclusively for detecting macroscopic discontinuities in structures after they have been in service for some time. It has become increasingly evident that it is practical and cost effective to expand the role of ultrasonic NDT testing to include all aspects of materials production and application. Research efforts are being directed at developing and perfecting NDT capable of monitoring (i) material production processes, (ii) material integrity following transport, storage and fabrication, and (iii) the amount and rate of degradation during service. In addition, efforts are underway to develop techniques capable of quantitative discontinuity sizing, permitting determination of material response using fracture mechanics analysis, as well as techniques for quantitative materials characterization to replace the qualitative techniques used in the past. Ultrasonic techniques play a prominent role in these developments because they afford useful and versatile methods for evaluating microstructures, associated mechanical properties, as well as detecting microscopic and macroscopic discontinuities in solid materials.

Ultrasonic measurements are widely used for elastic constant determination of anisotropic materials. Tomography is a powerful NDE tool that has seen a rapid development in last two decades. Tomography is image reconstruction of functions from multiple projections. In



tomography, two basic approaches are used to obtain the information required to reconstruct the generally complex propagation velocity distribution. These approaches can be classified as ray-tracing methods and wave-propagation methods. Both methods are based on approximate solutions of the wave equation, which governs the propagation of ultrasonic wave through media with inhomogeneous velocity distribution.

In Tomographic reconstruction, an object having some property distribution is inspected from a number of angles. These projections are then used to generate a distribution over a grid of cells, referred to as pixels, by superposition of all the projection at each pixel. Basically there are two types of reconstruction methods, viz., direct and iterative. The direct method can be further classified into direct algebraic methods and Fourier transform based methods. The iterative methods include various reconstruction techniques such as Algebraic Reconstruction Technique (ART), Simultaneous Iterative Reconstruction Technique (SIRT), Multiplicative Algebraic Reconstruction Technique (MART), and Entropy Optimization etc. These reconstruction algorithms are frequently applied to determine elastic constants of composite materials.

## **1.2 LITERATURE SURVEY**

The conventional tomographic problem may be described as the task of reconstructing an unknown scalar function from its projections. In a variety of applications, it has been successfully applied to get a scalar property distribution in a cross section, such as slowness distribution etc.

Synge [1] developed the theory of slowness surfaces after that Musgrave [2] first introduced the idea of superimposing the slowness surface on the geometric space, which contains the incident and emerging waves.

In the literature, only a few ray-tracing algorithm for wave propagation in anisotropic inhomogeneous materials are discussed. Silk [3] divides the austenitic weld region into a number of quadrilateral regions, each with a fixed direction of grain crystals. Ogilvy [4] defined the inhomogeneity of the weld by empirical analytic function that describes the orientation of grain crystals continuously.

More recently, Rokhlin et al. [5] have described a unified approach to the numerical solution of the reflection-refraction problem for generally anisotropic media. Ogilvy [6] also studied the influence of austenitic weld geometry and manufacture on ultrasonic inspection of weld joints. Ogilvy [7,8] was the first to propose a ray-tracing model for ultrasonic NDT in austenite welds. Schmitz et al. [9] modified the Ogilvy's model and proposed a new model for austenite materials to follow the longitudinal, horizontal and vertical polarized shear wave propagation from the base material through the cladding in three dimensions.

The treatment of anisotropy has been dealt with, by some researchers, for various applications. Thomson [10] presented simplified expressions for wave velocities in terms of anisotropic parameters and trigonometric functions. These expressions are appropriate for weakly anisotropic media (10-20 percent), occurring in geophysics applications. This weak anisotropy formulation was used by Stewart [11] in deriving Algebraic Reconstruction Technique (ART) correction for base velocity and anisotropic parameters. These ART corrections are applicable in case of cross hole imaging. This approach was later applied for tomographic reconstruction in rocks and polymer composites [12,13]. Kline and Wang [14] developed a modified versions of ART for composite materials. They used the governing equations for wave propagation in anisotropic material and composite micro mechanism to account for variation of acoustic velocity with propagation direction. This method requires a prior knowledge of properties of composite material constituents, that is, fibers and matrix. The time delay measurement of single wave mode was used for tomographic reconstruction. This technique was later extended to construct multiple material parameters using the time delay information of multiple independent modes of acoustic signal [15]. Generally when the time delay measurement multiple modes are considered, it is required to perform ray tracing for each mode independently. This makes it computationally intentional, as the method is iterative.

### **1.3 PRESENT WORK**

In this work, ray tracing technique is applied for tomographic image reconstruction to determine principal elastic constants and density of given specimen. Multi-parameter image reconstruction using ART algorithm is presented.

To ensure the reliability of ultrasonic inspection techniques, these complex material properties as well as the influence of micro structural inhomogeneities and the effects of non-planar surfaces and interfaces on ultrasonic wave propagation have to be taken in to account. In this respect, simulation and optimization in ultrasonic testing have gained a considerable importance, where mathematical modeling provides a simple method of assisting analysis. In this presentation a ray-tracing model is developed to follow quasi-longitudinal and quasi-shear wave propagation in composite materials for various phase angle, which is further applied to determine elastic constants and density of composite materials.

The present model is also used to reconstruct images using data obtained from Laser Based Ultrasonic (LBU) setup. Effect of various parameters on the performance of reconstruction model is evaluated.

## **1.4 THESIS ORGANISATION**

Chapter II gives the fundamentals of elastic wave propagation in anisotropic media and refraction principles based on Snell's law. It describes the equations of motion and plane wave solution of this equation. It discusses the fundamental equation of wave propagation in inhomogeneous and anisotropic media. Various terms associated with the elastic wave propagation in anisotropic media such as phase and group velocity, slowness, energy flux and critical angle are discussed in this chapter. Snell's law applied to anisotropic materials is also discussed.

Chapter III presents mathematical formulation of the ray tracing and then algorithm of two point ray tracing is discussed in detail. Then application of Edge detection on ray tracing algorithm is discussed.

Chapter IV presents the basic tomographic algorithms. Then application of tomography on determination of elastic constants and density is discussed.

Chapter V includes the results of application of tomographic image reconstruction model in determining elastic constants. Then experimental results based on experimental data obtained

from Laser ultrasonic set up are discussed. Then effect of various parameters on the performance of model is discussed.

Chapter VI presents the conclusion and scope of future work.

# **Basics of Ultrasonic wave propagation in anisotropic media**

## **2.1 INTRODUCTION**

Ultrasonics involves the propagation of acoustic waves. Therefore, it is necessary to understand the basic features of propagating waves and some of the mathematical equations governing wave propagation. Acoustics is the study of time-varying deformations, or vibrations in elastic media. It is concerned with material particles that are small but yet contain many atoms. Within each particle the atoms move in unison. Therefore, acoustics deals with macroscopic phenomena and is formulated as if matter were a continuum.

Propagation of ultrasonic waves in isotropic media has been well studied and can be predicted theoretically with good results. The problem is defined by two constants for the medium, such as  $\lambda$  and  $\mu$ , the Lamé constants and, the incident wave speed and direction. For anisotropic media the problem becomes considerably more complicated, as the elastic constants determining the wave propagation are then directionally dependent.

In general, for a given propagation direction, the wave equation has three solutions with differing speeds corresponding to three different polarization. A plane wave solution to the wave equation describes the possibility of three different wave modes with different phase velocities. These wave modes are not in general, purely longitudinal or transverse, but quasi wave modes.

The effect of anisotropy on ultrasonic wave propagation can be very marked as wave velocities become directionally dependent; group and phase velocities are no longer necessarily parallel or equal in magnitude. These effects lead to beam distortion with in the material, unexpected beam propagation directions, 'favoured' propagation directions, alteration in spatial profiles and, for inhomogeneous media, beam paths which become curved as the beam propagates through the material. It is therefore important to be able to

predict such effects to ensure that beam energy (which travels in the group velocity direction) is directed to the required region for inspection purpose. A brief review of wave propagation is presented. The basic concepts and formulations, included in this chapter are taken from[17].

## 2.2 EQUATION OF MOTION

The static equilibrium of an arbitrary, three-dimensional solid body occupying volume  $V$  that has both surface and body forces requires that the resultant force vector vanish, this gives

$$\frac{\partial \sigma_{ij}}{\partial x_j} + \rho b_i = 0 \quad i=1,2,3 \quad (2.1)$$

where  $\sigma_{ij}$  represents components of stress and  $\rho$  is density and  $b_i$  is the body force density vector. This is a static result, however, and to describe the dynamical motion of a continuum, an inertial term accounting for the particle acceleration must be included,

$$\frac{\partial \sigma_{ij}}{\partial x_j} + \rho b_i = \rho \frac{\partial^2 u_i}{\partial t^2}, \quad (2.2)$$

It is also called Cauchy's equation. If body force  $b_i$  vanishes for free, unforced motion, it gives

$$\frac{\partial \sigma_{ij}}{\partial x_j} = \rho \frac{\partial^2 u_i}{\partial t^2}, \quad (2.3)$$

and this gives dynamical equation of equilibrium for the elastic continuum. Using constitutive relations Eq. 2.3 can be written as

$$C_{ijkl} \frac{\partial \varepsilon_{kl}}{\partial x_j} = \rho \frac{\partial^2 u_i}{\partial t^2}, \quad (2.4)$$

where,  $C_{ijkl}$  is the elastic coefficient tensor. It is symmetric and positive definite in the sense that

$$C_{ijkl}n_{ij}n_{kl} \geq 0$$

for all symmetric  $n_{ij}$  where equality is satisfied only when  $n_{ij} \equiv 0$

By inserting for the strain  $\epsilon_{kl}$  its linearized equivalent in terms of the displacement gradient,

$$\epsilon_{kl} = \frac{1}{2} \left[ \frac{\partial u_k}{\partial x_l} + \frac{\partial u_l}{\partial x_k} \right], \quad (2.5)$$

Eq. (2.4) can be written as

$$\frac{1}{2} C_{ijkl} \frac{\partial}{\partial x_j} \left[ \frac{\partial u_k}{\partial x_l} + \frac{\partial u_l}{\partial x_k} \right] = \rho \frac{\partial^2 u_i}{\partial t^2}, \quad (2.6)$$

This can be written as

$$C_{ijkl} \frac{\partial^2 u_k}{\partial x_j \partial x_l} = \rho \frac{\partial^2 u_i}{\partial t^2} \quad (2.7)$$

Equation (2.7) is the equation of motion for an infinite linear elastic medium in three dimensions.

## 2.3 PLANE WAVE PROPAGATION IN BULK MATERIALS

The plane harmonic wave solution of Eq. (2.7) can be expressed either in index notation or in vector notation as

$$\mathbf{u}(\mathbf{r}, t) = A_0 \mathbf{p} \exp i(\mathbf{k} \cdot \mathbf{r} - \omega t) \quad (2.8)$$

$$u_j(x_m, t) = A_0 p_j \exp i(k_m x_m - \omega t) \quad (2.9)$$

where  $A_0$  is the amplitude of the wave,  $\mathbf{p}$  ( $p_j$ ) is the polarization unit vector and  $\omega$  is the angular frequency. The wavevector  $\mathbf{k}$  or  $(k_m)$  is given by

$$\mathbf{k} = k\mathbf{n}, \quad k = \frac{2\pi}{\lambda} \quad (2.10)$$

where  $\mathbf{n}$  is a unit vector in the direction of wave propagation, and  $\lambda$  is the wavelength. The phase of the wave  $\phi$  is given by

$$\phi = \mathbf{k} \cdot \mathbf{r} - \omega t \quad (2.11)$$

For points of constant phase on the wave is

$$\mathbf{k} \cdot \mathbf{r} - \omega t = \text{const.} \quad (2.12)$$

Taking differential and rearranging gives

$$\mathbf{k} \cdot \frac{d\mathbf{r}}{dt} = \omega \quad (2.13)$$

Substituting  $\mathbf{k}$  from Eq. (2.10) and let  $\xi$  be the projection of the wavefront position vector  $\mathbf{r}$  on the direction of wave propagation ( $\xi = \mathbf{n} \cdot \mathbf{r}$ ), as shown in Fig. 2.1,

$$k\mathbf{n} \cdot \frac{d\mathbf{r}}{dt} = \omega \quad (2.14)$$

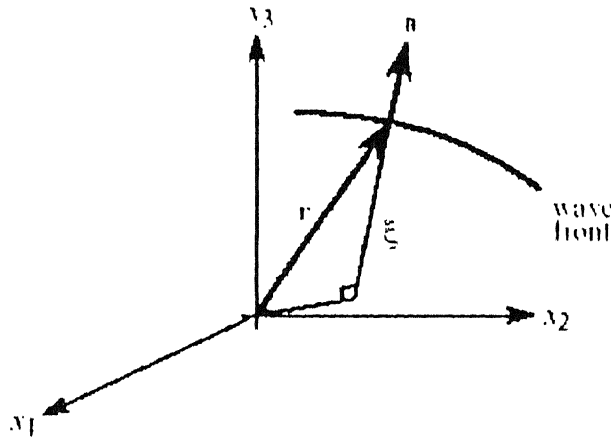


Figure 2.1 Wavefront moving in a rectangular coordinate system

and the propagation of a point of constant phase proceeds with phase velocity  $V$  given by

$$V = \frac{d\xi}{dt} = \frac{\omega}{k} \quad (2.15)$$

in vectorial form



$$\mathbf{V} = V\mathbf{n} = \frac{\omega}{k}\mathbf{n}. \quad (2.16)$$

Substituting the plane harmonic wave solution (2.9) into the equation of motion (2.7) gives

$$\rho\omega^2 u_i = C_{ijlm} k_j k_l u_m, \quad (2.17)$$

Or

$$C_{ijlm} n_j n_l u_m - \rho V^2 p_i = 0, \quad (2.18)$$

By using  $p_i = \delta_{im} p_m$ , the above equation can be rewritten as

$$(C_{ijlm} n_j n_l - \rho V^2 \delta_{im}) p_m = 0. \quad (2.19)$$

where  $\delta_{im}$  is the Kronecker delta. In order to have a nontrivial solution for  $p_m$ , the determinant of the coefficients for the linear equation Eq. (2.18) must vanish, leading to the following well known eigenvalue equation, also known as Christoffel's equation,

$$|C_{ijlm} n_j n_l - \rho V^2 \delta_{im}| = 0. \quad (2.20)$$

if  $\lambda_{il} = C_{ijlm} n_j n_l$  and  $\eta = \rho V^2$

Eq. (2.19) can also be written as

$$(\lambda_{il} - \eta \delta_{im}) p_m = 0 \quad (2.21)$$

From the properties of  $C_{ijlm}$ , it follows that  $\lambda_{il}$  is also symmetric and positive definite. Therefore, all the Eigen values of  $\lambda_{il}$  are real and positive and their corresponding eigenvectors are orthogonal.

This can be interpreted as that for a given direction of wave propagation  $\mathbf{n}$  there will be three phase velocities, and three corresponding displacement vectors will be orthogonal. These three waves are pure shear, quasi-longitudinal and quasi shear wave.

Pure longitudinal mode (the polarization vector  $\mathbf{p}$  is parallel to the propagation direction  $\mathbf{m}$ ,  $l, m, n$  are the direction cosines of propagation direction) is obtained only when  $p_i = n_i$  ( $i = 1, 2, 3$ ). Pure shear mode (the polarization vector  $\mathbf{p}$  is normal to the propagation direction  $\mathbf{n}$ ) are obtained only when  $p_1 n_1 + p_2 n_2 + p_3 n_3 = 0$  (i.e.  $\mathbf{p} \cdot \mathbf{n} = 0$ ). In all other cases, either quasi-longitudinal or quasi-shear modes can only propagate. It can also be noted that any general wave propagation can be split in three modes: pure shear (S), quasi-longitudinal (QL) and quasi-shear (QS). In an elaborate form Eq. (2.21) can be written as

$$\begin{bmatrix} \lambda_{11} - \rho V^2 & \lambda_{12} & \lambda_{13} \\ \lambda_{12} & \lambda_{22} - \rho V^2 & \lambda_{23} \\ \lambda_{13} & \lambda_{23} & \lambda_{33} - \rho V^2 \end{bmatrix} \begin{Bmatrix} p_1 \\ p_2 \\ p_3 \end{Bmatrix} = \begin{Bmatrix} 0 \\ 0 \\ 0 \end{Bmatrix} \quad (2.22)$$

where  $\lambda$  in terms of elastic constants can be given as

$$\begin{aligned} \lambda_{11} &= \ell^2 C_{1111} + m^2 C_{1212} + n^2 C_{1313} + 2mnC_{1312} + 2n\ell C_{1113} + 2m\ell C_{1112} \\ \lambda_{22} &= \ell^2 C_{1212} + m^2 C_{2222} + n^2 C_{2323} + 2mnC_{2223} + 2n\ell C_{2312} + 2m\ell C_{2212} \\ \lambda_{33} &= \ell^2 C_{1313} + m^2 C_{2323} + n^2 C_{3333} + 2mnC_{3323} + 2n\ell C_{3313} + 2m\ell C_{2313} \\ \lambda_{12} &= \ell^2 C_{1112} + m^2 C_{2212} + n^2 C_{2313} + mn(C_{2312} + C_{2213}) + n\ell(C_{1123} + C_{1312}) + m\ell(C_{1122} + C_{1212}) \\ \lambda_{13} &= \ell^2 C_{1113} + m^2 C_{2312} + n^2 C_{3313} + mn(C_{2313} + C_{3312}) + n\ell(C_{1133} + C_{1313}) + m\ell(C_{1123} + C_{1312}) \\ \lambda_{23} &= \ell^2 C_{1312} + m^2 C_{2223} + n^2 C_{3323} + mn(C_{2323} + C_{2233}) + n\ell(C_{3312} + C_{2313}) + m\ell(C_{2213} + C_{2312}) \end{aligned} \quad (2.23)$$

$m, l, n$  are the direction cosines of propagation direction

## 2.4 PHASE AND GROUP VELOCITY

Phase velocity is defined as the velocity with which plane wave crests and troughs travel through a medium and is expressed as the ratio of the frequency of vibration and the wave number (i.e. the number of wavelengths per unit distance normal to the wavefronts). Group

velocity, also known as ray or energy velocity, is defined as the velocity with which the energy of the wave propagates.

An additional complication in anisotropic media is that the wave normal does not necessarily coincide with the propagation direction of the energy (ray direction). An arbitrary wave is dependent on time and spatial coordinates as  $f = f(\omega t - \mathbf{k} \cdot \mathbf{x})$ . In dispersive media, where the velocity is dependent on frequency, the acoustic energy of a narrow-band tone-burst propagates at the group velocity  $V_g$ . The phase velocity is simply

$$V = \frac{\omega}{k}, \quad (2.24)$$

and the group velocity is given as

$$V_g = \frac{\partial \omega}{\partial k} \quad (2.25)$$

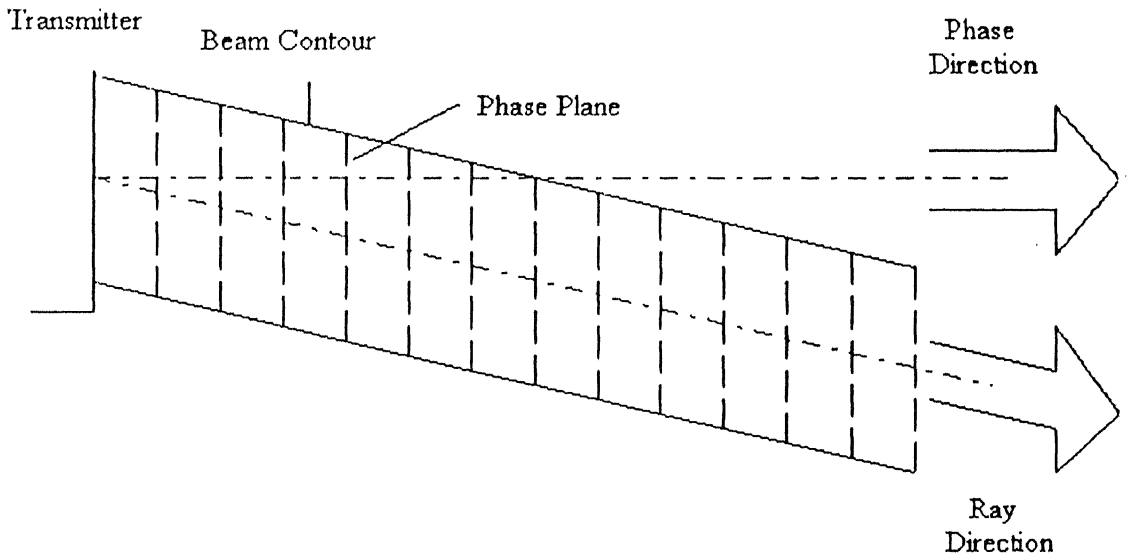


Figure 2.2 Deviaton between phase direction and ray direction

In the symmetry directions only pure modes propagate and the phase and ray directions are necessarily parallel. This is because deviation from a symmetry direction in any direction

must have the same effect as an equal deviation in the opposite direction. This also means that the velocities of pure waves are either maxima or minima for that particular mode. In any other directions the beam becomes skewed as illustrated in Figure 2.2. Needless to say that this skewing effect makes it more difficult to align the ultrasonic transducers for optimal inspection in highly anisotropic materials such as unidirectional composite laminates. The same effect is also responsible for the lateral shift of the transmitted ultrasonic beam through anisotropic plates that occurs even at normal incidence.

## 2.5 RELATION BETWEEN THE PHASE AND GROUP VELOCITIES

The group velocity can be written in terms of phase velocity as

$$V_{gi} = \frac{C_{ijkl} n_i p_m p_j}{\rho V} \quad (2.26)$$

In order to find the relation between  $V_g$  and  $V$  a vector  $Q$  is defined here as follows

$$Q_i = C_{ijkl} n_i p_m p_j \quad (2.27)$$

group velocity can be written as

$$V_{gi} = \frac{Q_i}{\rho V} \quad (2.28)$$

From the equation of motion

$$C_{ijkl} n_j n_l p_m p_i - \rho V^2 = 0. \quad (2.29)$$

This can be written as

$$Q_i n_i = \rho V^2 \quad (2.30)$$

Finally, from Eqs. (2.46) and (2.48),

$$V_g n_i = V \quad (2.31)$$

Or

$$V_g \cos \gamma = V, \quad (2.32)$$

where  $\gamma$  is the angle between  $V_g$  and  $V$ . This relation indicates that  $V$  is the projection of  $V_g$  in the direction of wave propagation

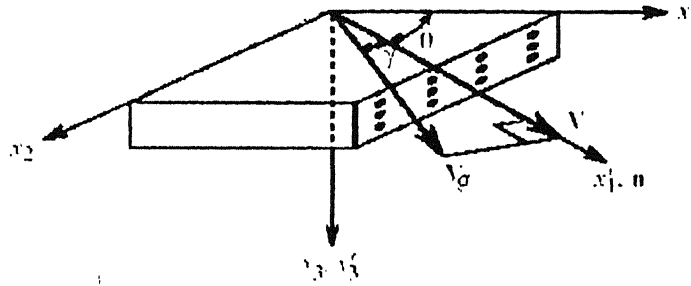


Figure 2.3 Relation between Phase velocity vector Group velocity vector

## 2.6 SLOWNESS SURFACE

An extremely useful insight of the effects of anisotropy can be obtained by examination of the slowness surfaces of a material. The correct interpretation of these surfaces can aid in the prediction of beam profiles in anisotropic materials.

The slowness vector of a wave,  $\mathbf{m}$ , is defined as

$$\mathbf{m} = \frac{\mathbf{n}}{V} \quad (2.33)$$

Hence  $\mathbf{m}$  has magnitude given by the reciprocal of the phase velocity. Since, for an anisotropic material, a wave's phase velocity magnitude is dependent on the phase velocity direction, it can be said that  $|\mathbf{m}|$  is a function of  $\mathbf{n}$ , i.e.

$$\mathbf{m} = \mathbf{m}(\mathbf{n}) \quad (2.34)$$

If the value of  $\mathbf{m}$  is plotted for all possible values of  $\mathbf{n}$ , i.e. all phase velocity direction, then a three-dimensional surface mapped out by the end points of the slowness vectors, is called slowness surface. Since there are three modes of wave propagation in anisotropic materials there exists three slowness surfaces corresponding to the three wave modes.

For an isotropic material each surface, corresponding to a wave polarization, will be a sphere since  $\mathbf{m}$  is independent of  $\mathbf{n}$  (i.e. phase velocity is independent of direction in isotropic materials)

Figure 2.6 shows a slice through the slowness surface for transversely isotropic. There are several points to notice from the figure

1. Each slowness surface is not a circle, indicating departure from isotropy.
2. The three slowness surfaces, one for each mode, are of different shapes. This immediately indicates that no two wave modes will behave in the same manner within the composite.

A further use of slowness surface arises in depicting group velocity i.e. energy direction. Theory shows that for any phase velocity direction  $\mathbf{n}$ , the normal to slowness surface for that particular value of  $\mathbf{n}$  is in the direction of the group velocity.

The usefulness of this unusual parameter than conventional velocity, lies in the nature of anisotropy itself. In many cases (e. g., refraction at a plane interface or diffraction from a periodic structure) the wave direction is determined by the wave speed. For example, according to the well-known Snell's law, the refraction angles of all reflected and transmitted waves are determined by the incident angle  $\theta_i$  and incident velocity  $V_i$  as

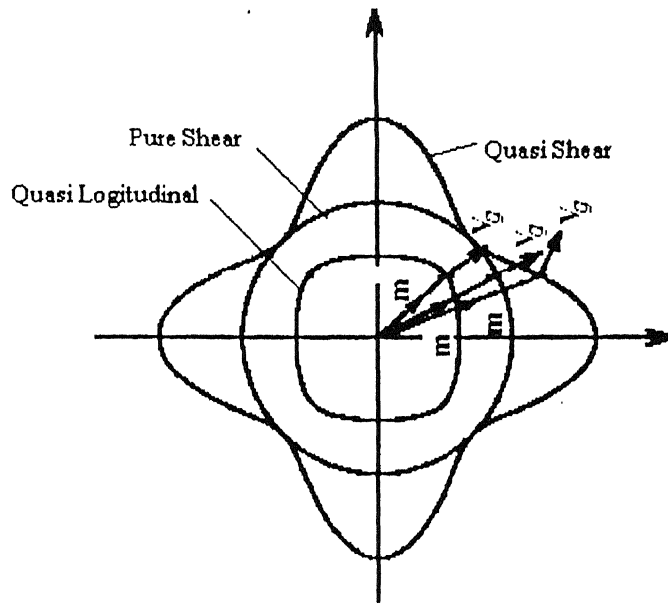


Figure 2.4 A general slowness diagram for an anisotropic material

follows

$$\frac{\sin \theta_r}{V_r} = \frac{\sin \theta_i}{V_i} \quad (2.35)$$

where the subscript  $r$  represents any of the refracted waves. This simple explicit relation for  $\theta_r$  becomes an implicit one for anisotropic cases

$$\frac{\sin \theta_r}{V_r(\theta_r)} = \frac{\sin \theta_i}{V_i(\theta_i)} \quad (2.36)$$

With slowness instead of velocity, the above condition becomes

$$m_r(\theta_r) \sin \theta_r = m_i(\theta_i) \sin \theta_i, \quad (2.37)$$

i.e., the projections of the slownesses of all waves are the same on the interface. This feature can be readily exploited to determine the refraction angles in a graphical way. At first the horizontal slowness projection  $m = m_i(\theta_i) \sin \theta_i$  is determined from the angle of incidence.

Then, for each particular refracted wave the refraction angle is determined from the intersection point of the slowness diagram with the same vertical line representing  $m$ . A special case in which the vertical line does not intersect a particular mode's slowness diagram then that mode will no longer exist in propagation.

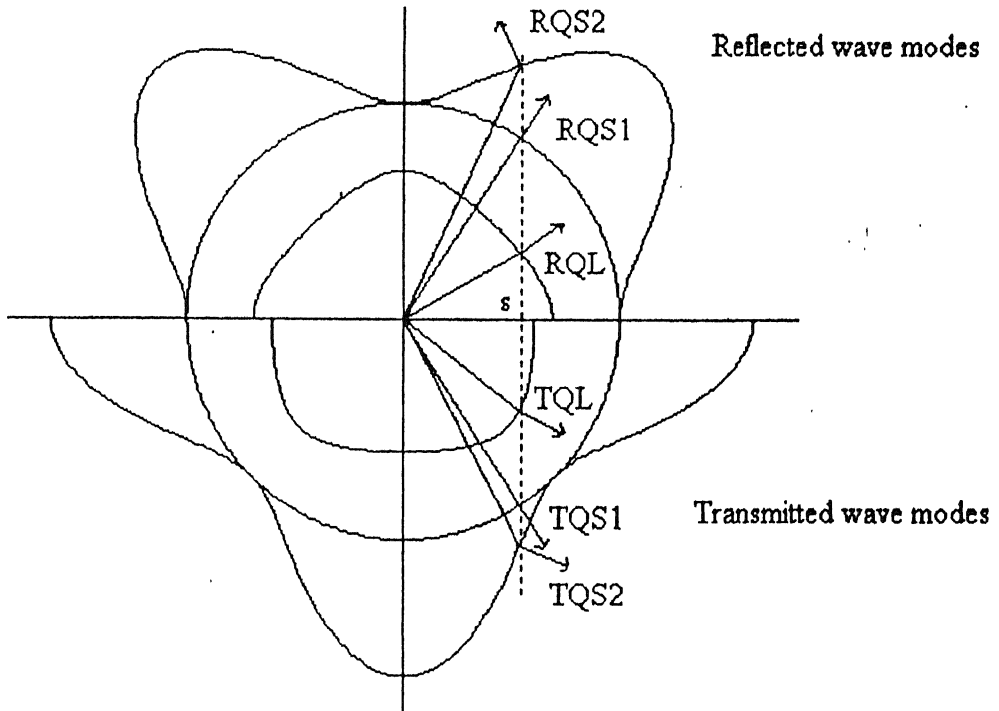


Figure 2.5 representation of reflected/transmitted wave modes using slowness diagram

## 2.7 FUNDAMENTALS OF REFLECTION AND REFRACTION

The simplest situation is depicted in Figure 2.6a, where a wave encounters a boundary at right angle or normal incidence. The interaction only involves reflection of some of the wave and transmission of a portion, with the amount of energy in each part depending on the material characteristics. A more complicated situation may arise, particularly in solids, when the wave strikes at an angle, or at oblique incidence. What may occur, as shown in Fig. 2.6b, is that two types of waves are reflected for a single incident wave. This phenomenon is known as mode conversion, and is illustrated for the case of a longitudinal wave generating both longitudinal and shear waves. Yet another aspect is involved when waves encounter edges. Complex scattering and diffraction of the waves may occur, similar to optics (figure 2.6c).



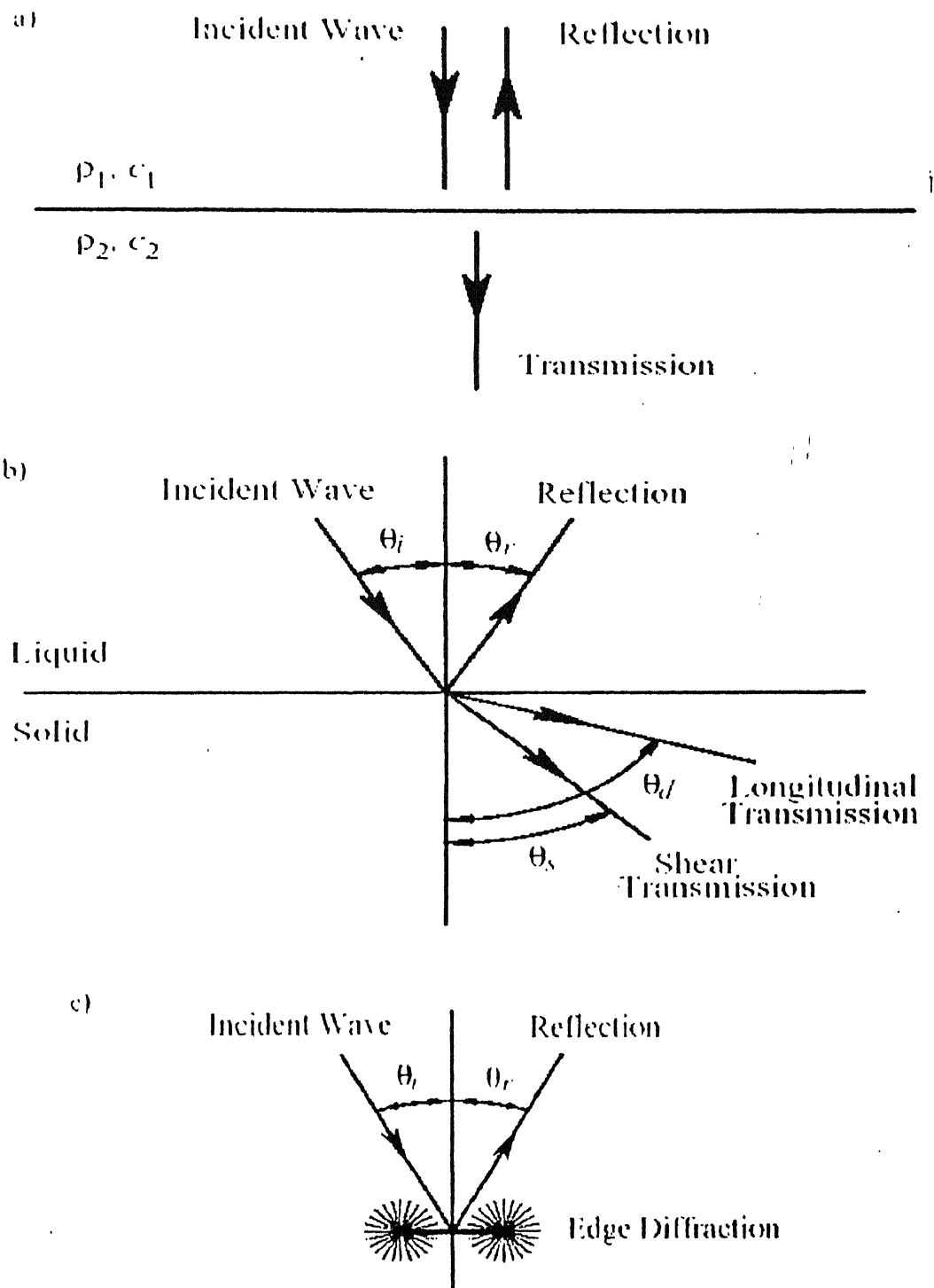


Figure 2.6 Different type of acoustic wave interaction with material discontinuities: (a) Normal Incidence (b) Oblique Incidence and Mode conversion (c) Diffraction and Scattering

## 2.8 SNELL'S LAW

Application of Snell's law for anisotropic materials can be understood by considering a monochromatic plane wave incident on the interface between two anisotropic solids as shown in Fig. 2.7 the interface coincide with  $x_1x_2$  plane and  $\mathbf{b}$  is a unit vector parallel to the  $x_3$ .

The displacement vector  $u_j$  of an elastic wave can be given as

$$u_j = A_0 p_j \exp[i(k_l x_l - \omega t)] \quad (2.38)$$

In terms of the previously defined slowness vector  $\mathbf{m}$ , the displacement vector can be also written in the following alternative form

$$u_j = A_0 p_j \exp[i\omega(m_l x_l - t)] \quad (2.39)$$

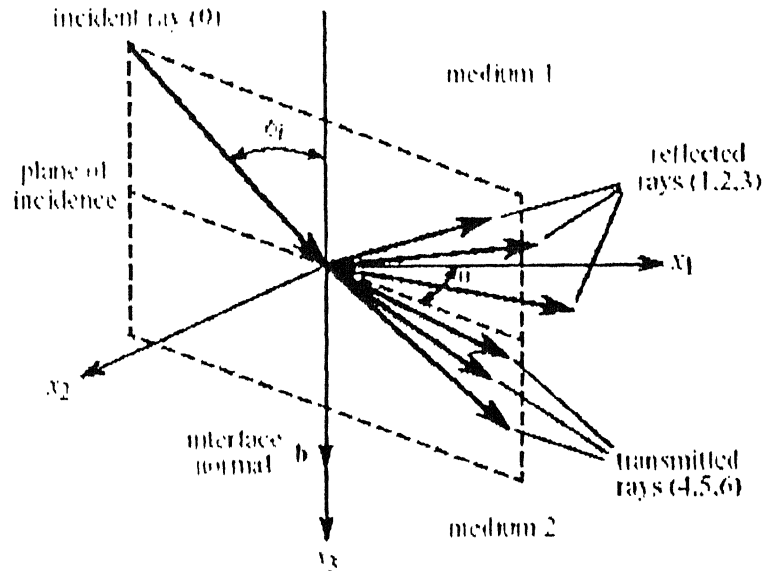


Figure 2.7 Acoustic wave incident on an interface between two anisotropic media

Because of assumed rigid boundary conditions at the interface, it requires continuity of both displacements and tractions across the boundary. Then, continuity of the displacements and tractions at the boundary ( $x_3 = 0$ ) is given by

$$u_l^0 + \sum_{\alpha=1}^3 u_l^\alpha = \sum_{\alpha=4}^6 u_l^\alpha \quad (2.40)$$

and

$$\sigma_{l3}^0 + \sum_{\alpha=1}^3 \sigma_{l3}^\alpha = \sum_{\alpha=4}^6 \sigma_{l3}^\alpha. \quad (2.41)$$

The incident wave is marked with superscript 0, and the three reflected and three transmitted waves are marked with superscripts 1; 2; 3 and 4; 5; 6, respectively.

Using the relevant displacement-strain and constitutive relationships, the stress tensor can be expressed as

$$\sigma_{ik} = C_{ikjm} \frac{\partial u_j}{\partial x_m} = i\omega m_m A_0 p_j \exp[i\omega(m_l x_l - t)] \quad (2.42)$$

Substituting Eq. (2.39) into (2.40) the displacement continuity (2.40) can be written as

$$A_0^0 p_j^0 \exp(i\omega m_l^0 x_l^0) = -\sum_{\alpha=1}^3 A_0^\alpha p_j^\alpha \exp(i\omega m_l^\alpha x_l^\alpha) + \sum_{\alpha=4}^6 A_0^\alpha p_j^\alpha \exp(i\omega m_l^\alpha x_l^\alpha), \quad (2.43)$$

Similarly Substituting Eq. (2.42) into (2.41) the stress continuity (2.41) can be written as

$$\begin{aligned} & m_m^0 C_{l3jm}^I A_0^0 p_j^0 \exp(i\omega m_l^0 x_l) \\ &= -\sum_{\alpha=1}^3 m_m^\alpha C_{l3jm}^I A_0^\alpha p_j^\alpha \exp(i\omega m_l^\alpha x_l) + \sum_{\alpha=4}^6 m_m^\alpha C_{l3jm}^{II} A_0^\alpha p_j^\alpha \exp(i\omega m_l^\alpha x_l), \end{aligned} \quad (2.44)$$

where  $C_{ikjm}^I$  and  $C_{ikjm}^{II}$ , are the elastic coefficients of the first and second media. The boundary conditions must be satisfied not only for all times  $t$ , which is a direct result of the common term  $\exp(i\omega t)$  in all equations, but also at all points ( $x_1, x_2, x_3 = 0$ ) on the interface. Since the exponential functions  $\exp(i\omega m_l^\alpha x_l)$  are linearly independent for  $\alpha = 0, 1, \dots, 6$  Eq. (2.43) and Eq. (2.44) will be satisfied only if all seven exponential functions are identically equal. Snell's law follows immediately from this simple fact since this condition requires that

$$m_l^0 x_l = m_l^1 x_l = m_l^2 x_l = m_l^3 x_l = m_l^4 x_l = m_l^5 x_l = m_l^6 x_l, \quad (2.45)$$

Here the coordinate vector  $\mathbf{x}$  lies on the interface plane therefore

$$\mathbf{b} \cdot \mathbf{x} = 0 \quad (2.46)$$

where  $\mathbf{b}$  is normal to the interface as shown in Fig. 4.5. Another way of looking at Eq. (2.45) is that for any two different  $\beta$  and  $\gamma$  values from the set  $(0, 1, \dots, 6)$

$$(\mathbf{m}^\beta - \mathbf{m}^\gamma) \cdot \mathbf{x} = 0. \quad (2.47)$$

Comparing Eqs. (2.46) and (2.47) shows that the difference  $\mathbf{m}^\beta - \mathbf{m}^\gamma$  is always parallel to  $\mathbf{b}$ , i.e., the plane defined by any two of the seven slowness vectors is always perpendicular to the interface. By definition, the slowness vector of the incident wave  $\mathbf{m}^0$  lies in the plane of incidence, therefore all the other surface vectors must also lie in the plane of incidence. Since the direction of the slowness vector coincides with that of the wave vector, it can be conclude that the wave vector of the incident wave as well as all the other wave vectors of the reflected and refracted waves lie in the same plane which is normal to the interface, i.e., the plane of incidence. Furthermore,

$$\begin{aligned} (\mathbf{m}^\beta - \mathbf{m}^\gamma) \times \mathbf{b} &= \mathbf{0} \\ \text{or, } \mathbf{m}^\beta \times \mathbf{b} &= \mathbf{m}^\gamma \times \mathbf{b}, \end{aligned} \quad (2.48)$$

i.e., all vector products of  $\mathbf{m}^\alpha$  are equal, which is an alternative form of Snell's law. This relationship can be converted into a more familiar form by introducing polar angles  $\phi^\alpha$  between the interface normal  $\mathbf{b}$  and the different wave normals  $\mathbf{n}^\alpha$  for the incident wave and all refracted and reflected waves so that  $\mathbf{b} \cdot \mathbf{n}^\alpha = \cos \phi^\alpha$ . Then, according to the definition of the vector product

$$\mathbf{m}^\alpha \times \mathbf{b} = m^\alpha \sin \phi^\alpha \quad (2.49)$$

Since  $\mathbf{b}$  is a unit vector and  $\alpha=1, 2, \dots, 6$ .

Equation (2.49) expresses generalized Snell's law for arbitrarily anisotropic media. It is important to note that the slowness values  $m^\alpha$  in general depend on the angles  $\theta^\alpha$  due to

anisotropy. Figure 2.8 illustrates the fundamental principle that slowness vector of the incident wave and all the other slowness vectors of the reflected and refracted waves lie in the same plane which is normal to the interface, i.e., the plane of incidence, and that they all have the same projection on the plane of the interface. The same conclusion holds for the projections of the wave vectors since  $k^\alpha = m^\alpha \omega$ . In terms of the wave vectors, we can summarize Snell's law as follows:

- The wave vectors for the incident and reflected/refracted waves all lie in a single plane, which also contains the interface normal and is called the incident plane.
- All their projections on the interface are equal.

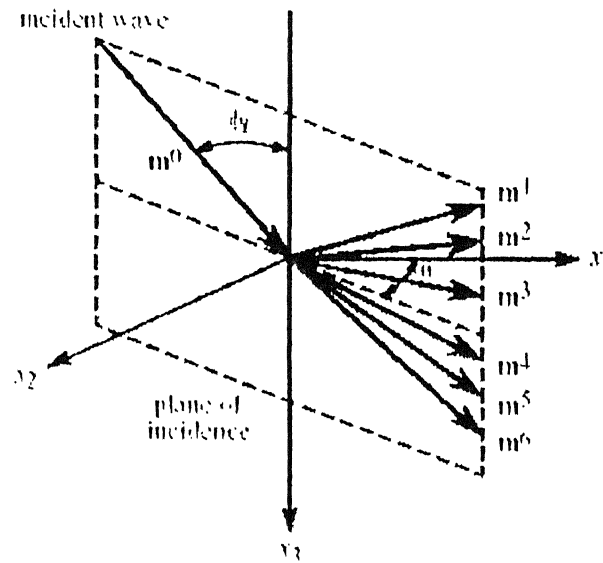


Figure 2.8 Generalized Snell's law for arbitrarily Anisotropic media

## 2.9 CLOSURE

In this chapter, basic concepts of ray propagation in anisotropic media has been discussed. Snell's law for refraction and reflection phenomena of ultrasonic waves at a planar interface has been discussed.

## CHAPTER 3 RAY TRACING

### 3.1 INTRODUCTION

Ray tracing is the most important part of a tomographic procedure. The accuracy and convergence of image reconstruction is solely dependent on resolution of the ray tracing procedure. In the present work, energy is assumed to behave as bundles of rays, each ray acting independently from its neighbors. As mentioned in previous Chapters, for anisotropic material, direction of energy propagation associated with each ray is generally not parallel to the phase velocity direction, the phase velocity defines the orientation of the phasefront associated with each ray. Furthermore, if a material is inhomogeneous then a ray path is likely to bend because of the continuous refraction as the ray experiences changing material properties.

For tomographic reconstruction, the information of the ray path followed by a ray between two specified positions is necessary. The two points generally represent transmitter and receiver position. The method of tracing the ray path between these two positions is known as two point ray tracing method.

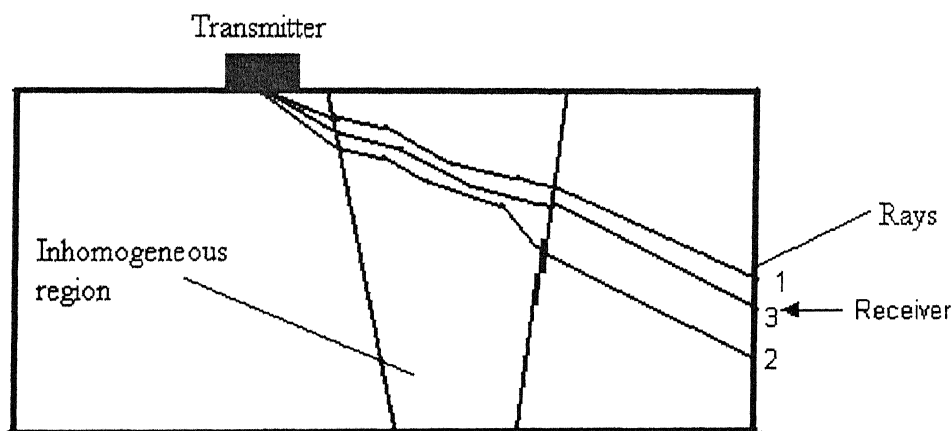


Figure 3.1 An example showing different iterations in a two point ray tracing method.

For example, if a defect is situated in a inhomogeneous material as shown in fig. 3.1, then determination of the ray path that reaches the defect edge will require two point ray tracing.

the defect edge, because of refraction at interfaces and bending in inhomogeneous material. As shown in Fig.3.1, a  $60^\circ$  (angle measured from surface normal) ray aimed at the top of a defect is skewed, refracted and bent away from the required endpoint. So for determining the route by which, energy will reach the defect requires the solution of a non-linear boundary value problem, (the boundary values being the required initial and final ray position, the non-linearity arising from the distortion of ray path within the material). As there is no general analytical technique exists for solving this problem. Numerical iterative techniques have to be employed to find an adequate solution to this problem. Although the use of iterative techniques are computationally intensive, they are generally versatile in the sense that arbitrary inhomogeneity may be considered and as many arbitrary combination of different materials can be taken.

### 3.2 THEORY

The basic concepts and formulation, included in this section are taken from [9]. In the absence of body forces, the equation of motion for the displacement vector  $\mathbf{u}$  in a homogeneous anisotropic solid reads as follows:

$$(\nabla \cdot \mathbf{C} \cdot \nabla) \cdot \mathbf{u}(\mathbf{R}, t) - \rho \frac{\partial^2}{\partial t^2} \mathbf{u}(\mathbf{R}, t) = 0 \quad (3.1)$$

and is explicitly dependent on space  $\mathbf{R}$  and time  $t$ . Here  $\nabla$  is the gradient vector,  $\rho$  is the material density.

The elastic stiffness tensor  $\mathbf{C}$  has the following structure:

$$\begin{pmatrix} \lambda_{||} + 2\mu_{||} & \nu & \nu & 0 & 0 & 0 \\ \nu & \lambda_{\perp} + 2\mu_{\perp} & \lambda_{\perp} & 0 & 0 & 0 \\ \nu & \lambda_{\perp} & \lambda_{\perp} + 2\mu_{\perp} & 0 & 0 & 0 \\ 0 & 0 & 0 & \mu_{\perp} & 0 & 0 \\ 0 & 0 & 0 & 0 & \mu_{\perp} & 0 \\ 0 & 0 & 0 & 0 & 0 & \mu_{||} \end{pmatrix} \quad (3.2)$$

If the grain direction is parallel to the  $x$ -direction, the elastic constants are given as

$$C_{11} = \lambda_{\parallel} + 2\mu_{\parallel}, \quad C_{22} = C_{33} = \lambda_{\perp} + 2\mu_{\perp}, \quad C_{44} = \mu_{\perp}, \quad C_{66} = \mu_{\parallel}, \quad C_{13} = \nu.$$

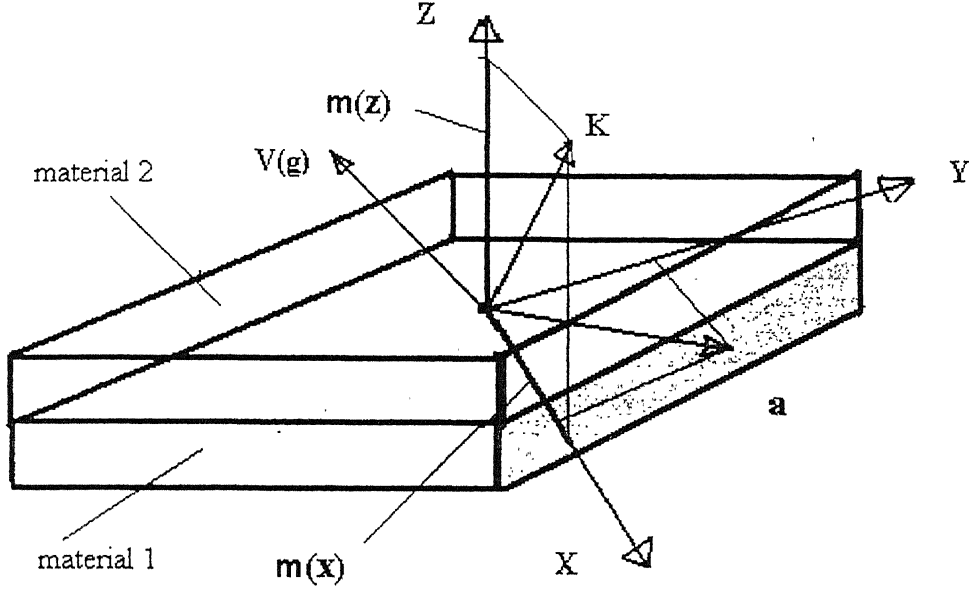


Figure 3.2 Fiber orientation , phase velocity and group velocity direction relative to cartesian coordinate system

The plane harmonic wave solutions of Eq. (3.1) are:

$$u_{\alpha}(R, \omega) = U \hat{u}_{\alpha} \exp[j\omega s_{\alpha} R] \quad (3.3)$$

where  $\omega$  is the circular frequency,  $\hat{u}_{\alpha}$  are the polarization vectors,  $m_{\alpha} = \hat{m}/V_{\alpha}$  is the slowness vector that shows the direction of phase propagation  $\hat{m}$  with a value inverse to the value of the phase velocity  $V_{\alpha}$ . The abbreviations  $\alpha$ =SH, qSV, qL denote SH-shear horizontal wave, qSV-quasi shear vertical wave, qL-quasi longitudinal wave. Solving the corresponding linear algebra problem leads to two dispersion relations:

$$m_s^2 [\mu_T + (\mu_L - \mu_T)(\underline{a} \cdot \hat{\mathbf{K}})^2] = \rho, \quad (3.4)$$

$$m_{qS, qL}^2 = \rho(B \pm (B^2 - 4A)^{1/2})/(2A), \quad (3.5)$$



where,

$$A = \mu_L(\lambda_T + 2\mu_T) + (\underline{\mathbf{a}} \cdot \hat{\mathbf{K}})^2(\lambda_L(\lambda_T + 2\mu_T) - \nu(\nu + 2\mu_L)) + (\underline{\mathbf{a}} \cdot \hat{\mathbf{K}})^4[(\lambda_L + 2\mu_L)(\mu_L - (\lambda_T + 2\mu_T)) + (\nu + \mu_L)^2], \quad (3.6)$$

$$B = \mu_L + \lambda_T + 2\mu_T + (\underline{\mathbf{a}} \cdot \hat{\mathbf{K}})^2(\lambda_L + 2\mu_L - (\lambda_T + 2\mu_T)). \quad (3.7)$$

The direction of the energy transport or the group velocity direction is

$$(\underline{\mathbf{V}}_g)_\alpha = V_\alpha \hat{\mathbf{K}} + F_\alpha V_\alpha (\underline{\mathbf{a}} \cdot \hat{\mathbf{K}})(\underline{\mathbf{I}} - \hat{\mathbf{K}}\hat{\mathbf{K}}) \cdot \underline{\mathbf{a}} \quad (3.8)$$

$$F_S = \frac{\mu_L - \mu_T}{\mu_T + (\mu_L - \mu_T)(\underline{\mathbf{a}} \cdot \hat{\mathbf{K}})^2} \quad (3.9)$$

$$F_{qs,ql} = \frac{1}{2} \left( y_A + 2(\underline{\mathbf{a}} \cdot \hat{\mathbf{K}})^2 z_A \pm \frac{F_1 - (\underline{\mathbf{a}} \cdot \hat{\mathbf{K}})^2 F_2}{\sqrt{B^2 - 4A}} \right) \quad (3.10)$$

$$y_A = \lambda_L(\lambda_T + 2\mu_T) - \nu(\nu + 2\mu_L) \quad (3.11)$$

$$z_A = (\lambda_L + \mu_L)(\mu_L - (\lambda_T + \mu_T)) + (\nu + \mu_L)^2$$

$$F_1 = [\mu_L^2 - (\lambda_L + 2\mu_L)(\lambda_T + 2\mu_T)][\mu_L - (\lambda_L + 2\mu_T)] - (\nu + \mu_L)^2(\mu_L + \lambda_T + 2\mu_T) \quad (3.12)$$

$$F_2 = F_1 + [\mu_L^2 - (\lambda_L + 2\mu_L)(\lambda_T + 2\mu_T)][\mu_L - (\lambda_L + 2\mu_T)] - (\nu + \mu_L)^2(\mu_L + \lambda_L + 2\mu_L) \quad (3.13)$$

As obtained from Eq. (3.8), the direction of the group velocity  $\hat{\mathbf{V}}_g$  differs from the phase direction  $\hat{\mathbf{m}}$  by an additional vector that corresponds to the projection  $\underline{\mathbf{a}}$  onto the plane perpendicular to  $\hat{\mathbf{m}}$ .

The sign ‘ + ’ in Eqs. (3.5) and (3.10) corresponds to the quasi-vertical polarized shear wave qSV, and ‘ - ’ to the quasi-longitudinal wave qL, respectively. Because of symmetric configurations it is sufficient to consider the wave propagation in the  $xz$ -plane. According to Snell’s Law, all projections of slowness vector  $\mathbf{m}$  onto the interface must be equal

$$m_x^I = m_x^{R\alpha} = m_x^{T\alpha}, \quad (3.14)$$

and their  $y$ -components absent

$$m_y^I = m_y^{R\alpha} = m_y^{T\alpha} = 0, \quad (3.15)$$

Under these conditions, the  $m_z^{R\alpha}$  components can be determined from the dispersion relations Eqs. (3.4) and (3.5) or the reflected/refracted SH-wave, we have

$$m_z^{R,TS} = (-b_s \pm \sqrt{(b_s^2 - a_s c_s)}) / a_s \quad (3.16)$$

$$a_s = \mu_T + (\mu_L - \mu_T) a_z^2 \quad (3.17)$$

$$b_s = (\mu_L - \mu_T) a_x a_z^2 s_x \quad (3.18)$$

$$c_s = [\mu_T + (\mu_L - \mu_T) a_x^2] s_x^2 - \rho \quad (3.19)$$

For qS and qL waves, the  $m_z^{R,Tq\beta}$  ( $\beta = S, L$ ) components of the slowness vector are defined as the roots of a fourth order polynomial

$$\begin{aligned} & (m_z^{q\beta})^4 (a_q + b_q a_z^2 + c_q a_x^4) + (m_z^{q\beta})^3 \cdot 2a_x a_z m_x (b_q + 2c_q a_z^2) \\ & + (m_z^{q\beta})^2 (m_x^2 [2a_q + b_q (a_x^2 + a_z^2) + 6c_q a_x^2 a_z^2] + d_q + e_q a_z^2) \\ & + (m_z^{q\beta}) \cdot 2a_x a_z m_x (m_x^2 (b_q + 2c_q a_x^2) + e_q) \\ & + m_x^4 (a_q + b_q a_x^2 + c_q a_x^4) + m_x^2 (d_q + e_q a_x^2) + f_q = 0 \end{aligned} \quad (3.20)$$

where

$$a_q = \mu_L (\lambda_T + 2\mu_T) \quad (3.21)$$

$$b_q = \lambda_L (\lambda_T + 2\mu_T) - \nu (\nu + 2\mu_L) \quad (3.22)$$

$$c_q = (\lambda_L + \mu_L) (\mu_L - (\lambda_T + 2\mu_T)) + (\nu + \mu_L)^2 \quad (3.23)$$

$$d_q = -\rho (\mu_L + \lambda_T + 2\mu_T) \quad (3.24)$$

$$e_q = -\rho(\lambda_L + 2\mu_L - (\lambda_T + 2\mu_T)) \quad (3.25)$$

$$d_q = \rho^2 \quad (3.26)$$

To separate the roots corresponding to qSV-wave and qL-wave, the dispersion relation Eq. (5) is transformed with two conditions

$$\frac{2A}{\rho} m_{qs}^2 - B \geq 0 \quad (3.27)$$

$$\frac{2A}{\rho} m_{qL}^2 - B \leq 0 \quad (3.28)$$

The corresponding group velocity vector for the refracted and reflected waves has to point from the interface into the respective material. If a root's pair from Eq. (3.27) or Eq. (3.28) is complex, a surface wave will occur and  $m_z^{R\alpha} = 0$ .

### 3.3 RAY TRACING ALGORITHM

The ray tracing algorithm follows Ogiliv's [9], with the exception for the selection of the boundary for the ray refraction at ray propagation interval (step 4). The procedure has to be followed as described.

1. For the given Transmitter and Receiver positions, find the group velocity angle, for the ray, which will reach Receiver position directly if specimen has no defects.
2. Find the phase angle using equations 3.8-3.13, for the group velocity angle, using iterative procedure. find the group velocity direction and the grain orientation.
3. Step one time interval forward in the group velocity direction and check that no region change has occurred.
4. If the region changes, reduce the time interval to reach the interface between regions and continue with step 5.
5. In the interface, determine the defect boundary, approximate it as a curve. Calculate the new phase velocity directions using equations Eqs. (3.15)–(3.16), (3.20).

6. Return to step 2 and repeat until the specimen boundary is reached.
7. If distance between final position and receiver position is less than considered accuracy-, then terminate, else continue with step 1.

### 3.4 EDGE DETECTION

As the ray reaches interface boundary, the information about the defect boundary is required. According to Snell's law, projection of slowness vector on to interface must be equal. To identify the interface boundary, all the neighbor pixels to the interface pixel, are taken, and then pixels present in interface boundary are identified. Interface boundary is identified by material properties of the pixels. A curve, passing through these pixels, is approximated.. Then equation of tangent to the curve is calculated. All projections are considered along the tangent. Figure 3.3 shows tangent to the curve at the interface pixel on interface boundary.

Figure 3.4 shows magnified view of the interface boundary. Pixels at interface are shown by blue line .Red line shows the approximated curve.

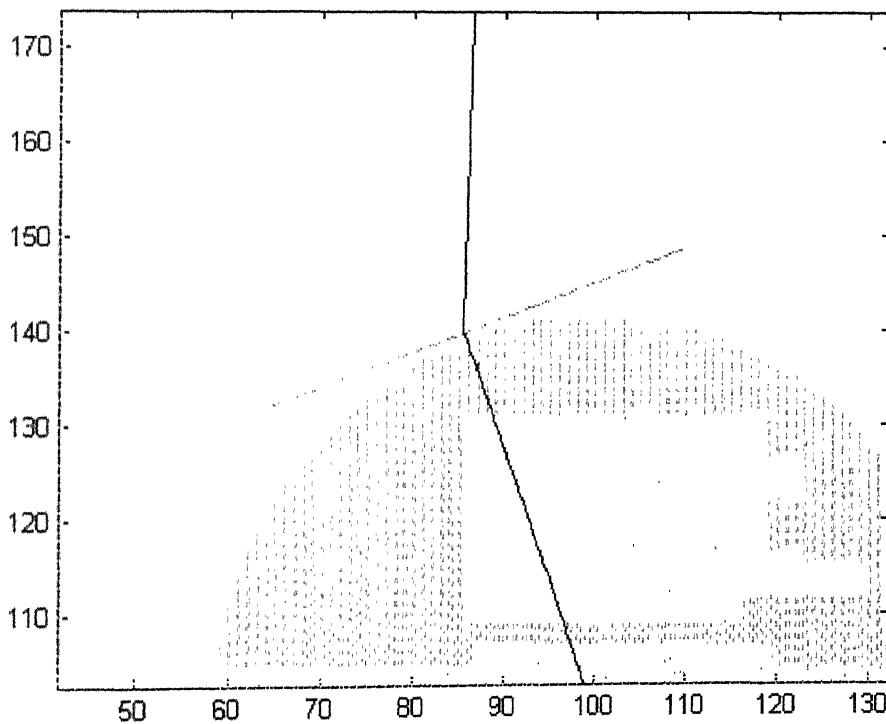


Figure 3.3 Edge detection

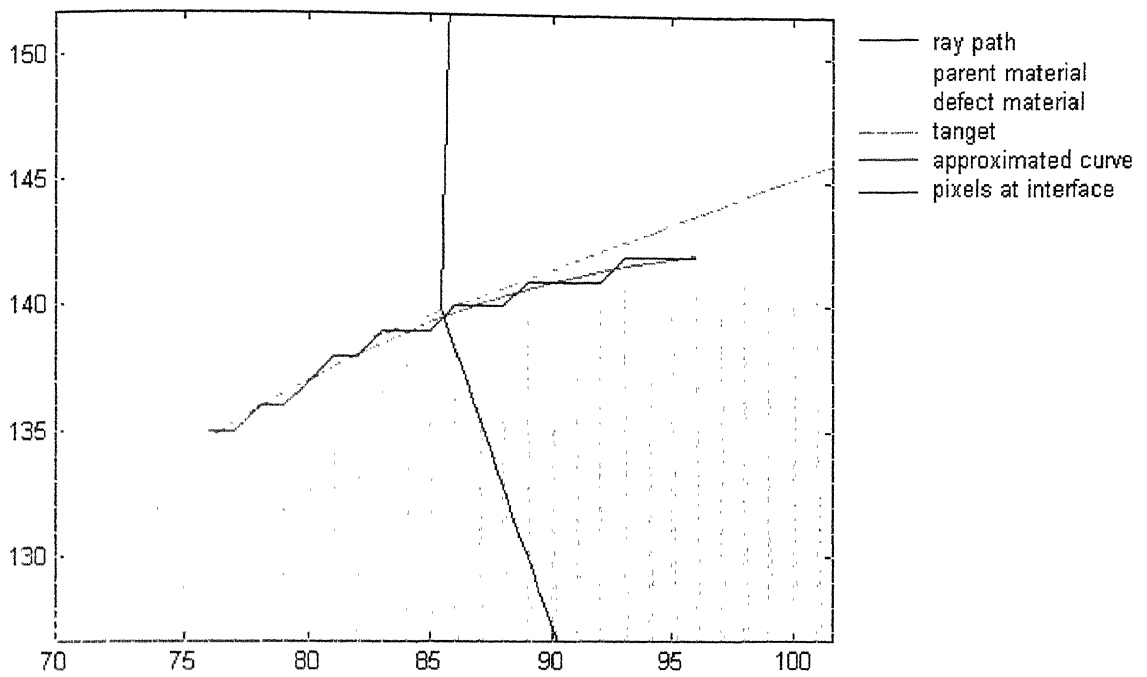


figure 3.4 Detection of interface boundary

### 3.5 CLOSURE

In this Chapter, basic concepts related to ray tracing are discussed. Then basic steps involved in the algorithm have been discussed. The process of edge detection is described.

## CHAPTER 4

# TOMOGRAPHY

### 4.1 INTRODUCTION

Tomography is a method of reconstructing a function from a set of its projections. These projections are line integrals of the unknown function computed along certain prescribed directions. Data in the form of line integrals arise naturally in measurements involving radiation sources as probes.

Tomographic algorithms are broadly classified as

1. Transform methods – these are direct and hence computationally efficient, but require a large number of projections to recover the solution with some degree of accuracy.
2. Series expansion method – these can produce meaningful answers with a fewer number of projections, but they are iterative and computationally intensive.
3. Optimization methods – the optimization approach requires the selection of a suitable functionals that has to be extremized, under the constraint of the experimentally recorded projections. The performance of this method in terms of accuracy and speed depends on quantity to be optimized.

### 4.2 CONVENTIONAL ART ALGORITHM

In tomography, projection data ( $p$ ) represents an integrated information resulting from interaction of source radiation with the material, and is expressed as [11]

$$p = \int_s f(x, y) ds \quad (4.1)$$

where  $f(x, y)$  and  $p_i$  are usually taken to be the slowness field in the object and time-of-flight (TOF) respectively. Here  $s$  represents the ray path of the ray.

The iterative reconstruction methods of tomography are based on the discretization of the cross sectional plane by a square grid. The length of the intercept of an  $i^{th}$  ray with the  $j^{th}$

pixel in a given projection is called the weight function ( $w_{ij}$ ). If  $f_j$  is the field value in the  $j^{th}$  pixel, the  $i^{th}$  projection is given as

$$p_i = \sum_{j=1}^N w_{ij} f_j \quad i=1,2,\dots,M \quad (4.2)$$

where M is the total number of rays and N is the number of pixels.

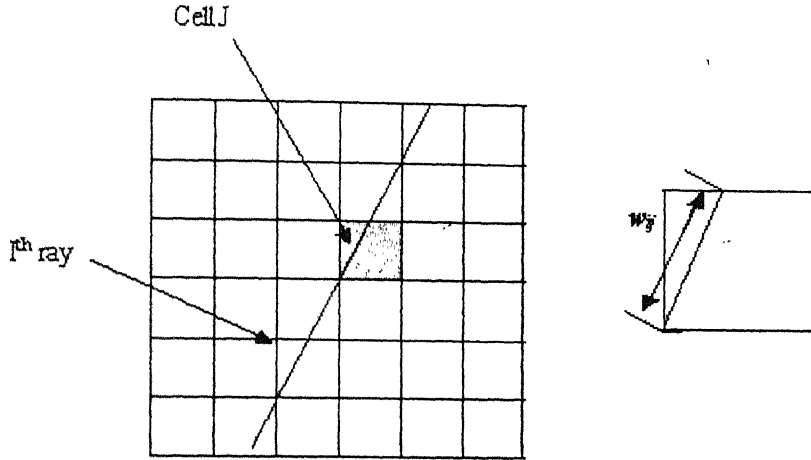


Figure 4.1 Weight function  $w_{ij}$  for  $i^{th}$  ray and  $j^{th}$  pixel.

It is required to collect the projection data over a number of view angles to carry out tomographic reconstruction. When ultrasound wave is used as a source radiation,  $f(x,y)$  and  $p_i$  are usually taken to be the slowness field (inverse of sound velocity) in the object and time-of-flight (TOF) respectively. The aim in tomography is to obtain  $f(x,y)$  from given  $p_i$ . The conventional algebraic reconstruction technique (ART) involves four major steps:

1. initial assumption of object field
2. calculation of correction
3. application of the correction
4. test for convergence

The word “convergence” is used here as a stopping criterion. It is not used in the strict mathematical sense, where a formal proof is required to show that the solution obtained

numerically is the real solution. Typically, in Gordon ART, the field values  $f_j$  in pixels are updated for  $k^{th}$  iteration using correction term as

$$f_j^k = f_j^{k-1} + \lambda w_{ij} (p_i - \langle w^i, f^{k-1} \rangle) / (w^i, w^i) \quad (4.3)$$

where  $\langle \rangle$  represents dot product,  $\lambda$  is relaxation parameter and  $w^i$  is a vector of intercepts or weights along  $i^{th}$  ray.

In isotropic materials, the field value  $f_j$  in a pixel gets updated from all the rays passing through that pixel and thus, each has a unique  $f_j$ , irrespective of direction of ray.

In case of anisotropic materials, the field value  $f_j$  is directionally dependent, for example, sound velocity in composite materials. So, the value  $f_j$  in one direction cannot be modified by the correction term of ray in another direction. Hence, the field  $f(x,y)$  is expressed as a function of direction,  $\theta$  and a set of independent parameter  $X$ . It is analogous to representing the velocity in composite materials as a function of their elastic constants and the direction of ray. Also Eq(4.2) is modified for anisotropic materials to ,

$$p_i = \sum_{j=1}^N w_{ij} \tilde{f}_{j,i}(X_j, \theta_i) \quad (4.4)$$

where  $\tilde{f}_{j,i}$  is the field value in  $j^{th}$  pixel along  $i^{th}$  ray, for direction  $\theta_i$  and  $x_j$  is a vector of independent parameter for pixel  $j$ . These projection data  $p_i$  are a result of interaction of component of the field function  $f(x,y)$  with the source radiation along the direction  $\theta_i$ . Thus, the problem of tomographic reconstruction for anisotropic materials reduces to the reconstruction of  $X$  in place of  $f(x,y)$ .

### 4.3 MART ALGORITHMS

The difference between ART and MART algorithms lies in the manner in which the corrections are applied to guessed field values. The corrections are additive in former, while multiplicative in the latter. These algorithms are essentially iterative in nature, but



intermediate steps may also involve repetitive calculations in the form of FOR loops. To identify the iterative loop, start and close labels with statement numbers have been indicated in the description of each algorithm.

The MART algorithms are first summarized. Let  $\phi_{i\theta}$  be the projection due to  $i^{\text{th}}$  ray in  $\theta$  direction of projection and  $\tilde{f}_i$  be the initial guess of the field value. The projection  $\tilde{\phi}_{i\theta}$  using the current field value can be obtained numerically [20] as

$$\tilde{\phi}_{i\theta} = \sum_{j=1}^N w_{i\theta j} f_j \quad i\theta = 1, 2, \dots, M_\theta \quad (4.5)$$

where  $M_\theta$  represents number of rays along the  $\theta$  direction. The parameter to be varied in each loop is indicated in brackets.

Start: 1 Start iterations (k):

Start: 2 For each projection angle ( $\theta$ ):

Start:3 For each ray ( $i\theta$ ):

Compute the numerical projection {Eq(4.4)}

Calculate the correction as :

$$\Delta\phi_{i\theta} = \phi_{i\theta} / \tilde{\phi}_{i\theta}$$

Start:4 For each cell ( $j$ )

If  $w_{i\theta j}$  is nonzero then :

MART1:

$$f_j^{\text{new}} = f_j^{\text{old}} \times (1.0 - \mu \times (1 - \Delta\phi_{i\theta})) \quad (4.6)$$

MART2:

$$f_j^{\text{new}} = f_j^{\text{old}} \times [1.0 - \mu \times \{w_{i\theta j} / (w_{i\theta j})_{\max}\} - (1 - \Delta\phi_{i\theta})] \quad (4.7)$$

MART3:

$$f_j^{\text{new}} = f_j^{\text{old}} \times (\Delta\phi_{i\theta})^{(\mu w_{i\theta j} / (w_{i\theta j})_{\max})} \quad (4.8)$$

where  $\mu$  is relaxation factor.

close:4

close:3

close:2

Check for convergence as:

If

$$\text{abs}[(f^{k+1} - f^k)/f^{k+1}] \times 100 \leq e$$

where  $e$  is a suitable stopping criterion. STOP:

Else : Continue

Close: 1

Step 3 and 4 form the essence of the reconstruction algorithm. All three versions include the relaxation factor  $\mu$ . Typical values for relaxation factor reported are in the range 0.01-0.1, larger values leading to divergence. It is to be noted that correction calculated in step 3 is the ratio of the recorded projection data ( $\phi_{i0}$ ) and that calculated from guessed field namely, ( $\phi_{i0}$ ), which is being iterated. The three versions of MART differ in the manner in which the corrections are implemented. In MART1, the weight function is prescribed in binary form, being unity if a pixel ray passes through a pixel and zero otherwise. In MART2 and MART3, the weight function is calculated precisely as the ratio of the length of the ray intercepted by the pixel and the maximum dimension of pixel enclosed in it.

#### 4.4 TOMOGRAPHY AS APPLIED TO COMPOSITE MATERIALS

Tomographic image reconstruction process can be applied to determine various elastic constants of orthotropic composite materials. The process is better known as vector tomography. In vector tomography, more than one parameters, in vector form are considered for tomographic reconstruction. These parameters are mainly elastic constants, density and fiber orientation. Minimum number of projections through each pixel should be equal or more than parameters considered for reconstruction. Through the difference in time of flight data in actual and estimated ray path, correction is applied on group velocity for all view angles considered. A system of nonlinear equation is obtained in terms of group velocity and elastic material properties. Corrected material properties are determined by solving the system of nonlinear equations. The process is repeated for ? till convergence criteria is satisfied. The method is used for determination of principal

elastic constants, mainly  $C_{11}$ ,  $C_{22}(=C_{33})$  and density. The algorithm for the process is as follows:

**Step 1. Initial assumption of object field .**

- Input time of flight data and initial guess for elastic constants. Decide convergence criteria.

**Step 2. Calculation of correction**

Start 1 For each view angle

- Start2 For each ray
- Assume view angle for the ray as group velocity angle.
- Find phase angle for given group velocity angle using equation 3.8.
- Perform two-point ray tracing for given transmitter position and receiver position
- Find intercepts for each pixel, present in the ray path.
- Find group velocity correction for each pixel, using ART algorithm(eq 4.3).

Close 2

Close 1

**Step 3 Application of correction**

Start 1 For each pixel

- Solve for elastic constants, using least square nonlinear method.

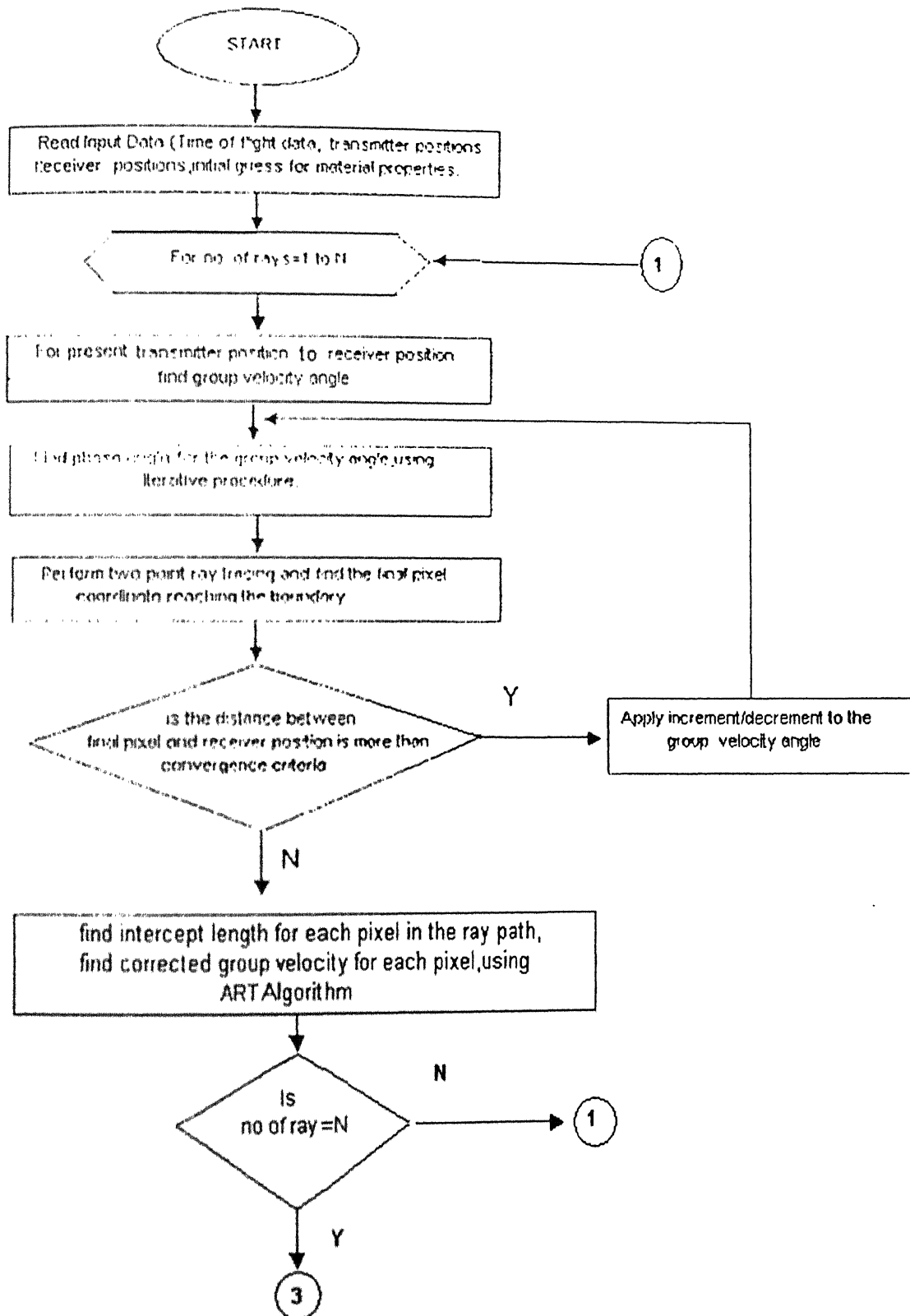
Close1

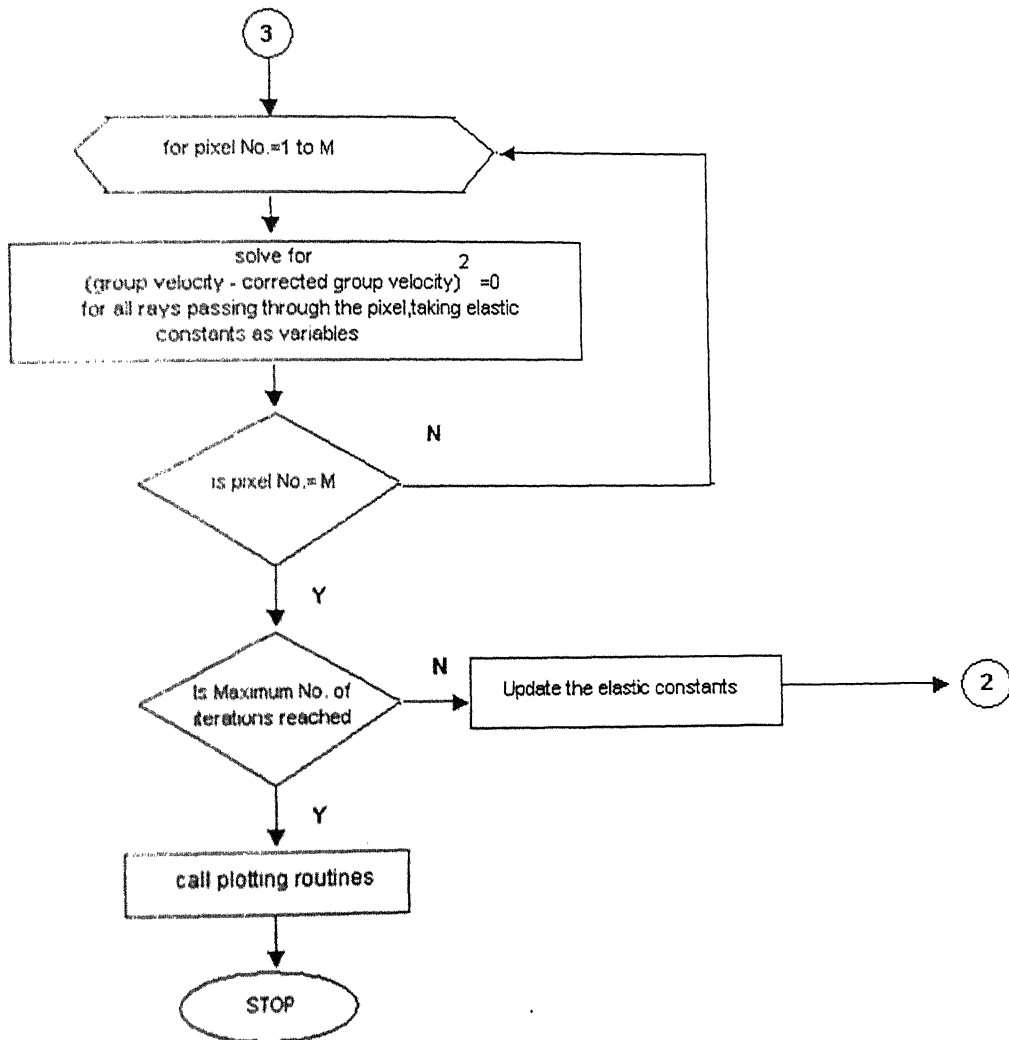
**Step 4 Test for convergence**

- If average error is less than convergence criteria or iteration is less than maximum number of iterations continue with step 1 else stop.

In step 3, to solve a system of nonlinear equations, MATLAB inbuilt function 'fsolve', is used . The program is written in MATLAB having 16 function files and around 2400 lines of executable statements. A detailed documentation of the program and various subroutines is given in Appendix A. In the next section a detailed flow chart is presented for the present work.

## 4.5 FLOW DIAGRAM FOR TOMOGRAPHIC IMAGE RECONSTRUCTION PROGRAM





## 4.6 CLOSURE

In this chapter various tomography algorithms are discussed. Then process of elastic constant determination is discussed and a detailed flow chart for the developed model is included.

## Chapter 5

### Results and Discussions

In this chapter, the results of tomographic reconstruction in inhomogeneous and anisotropic materials are presented. The results consist of reconstruction images developed by the present model for different materials.

The present two-dimensional model is applied to identify the parent and defect materials in a given specimen using time of flight data. The tomographic algorithm is also applied to experimental time of flight data, to determine the material properties of given specimen. The input parameters for image reconstruction are time of flight data and initial guess. Relaxation parameter considered for all reconstruction is 1.0.

#### 5.1 RECONSTRUCTION USING SIMULATED DATA

Time of flight data consists of transmitter position, receiver position and corresponding time of flight. Pixel size considered for tomography is  $1 \times 1$  mm and for ray tracing it is  $0.1 \times 0.1$  mm. Edge detection is applied to find the interface when ray goes from one material to another material.

Tomographic reconstruction for rectangular, elliptical and circular defect is presented using simulated data. To obtain simulated time of flight data, correct material properties are assigned to each pixel and then ray tracing is performed for different view angles. The calculated time of flight data is used as an input to tomographic reconstruction algorithm. Figure 5.1 shows the ray tracing performed on the specimen with rectangular defect for one of its view angles considered. Material properties for parent and defect material are given in section 5.1.1. Transmitter positions for the rays are along z-axis and x-axis and corresponding receiver positions are along  $z = 200$  and  $x = 200$  lines. The bending of ray can be observed, as it enters into defect. The change in group velocity angle is dependent on properties of parent and defect material, incident angle and defect boundary.

##### 5.1.1 Rectangular defect

Tomographic reconstruction is applied to construct the images of a specimen with rectangular defect. The size of the specimen is  $20 \times 20$  mm. The parent material is

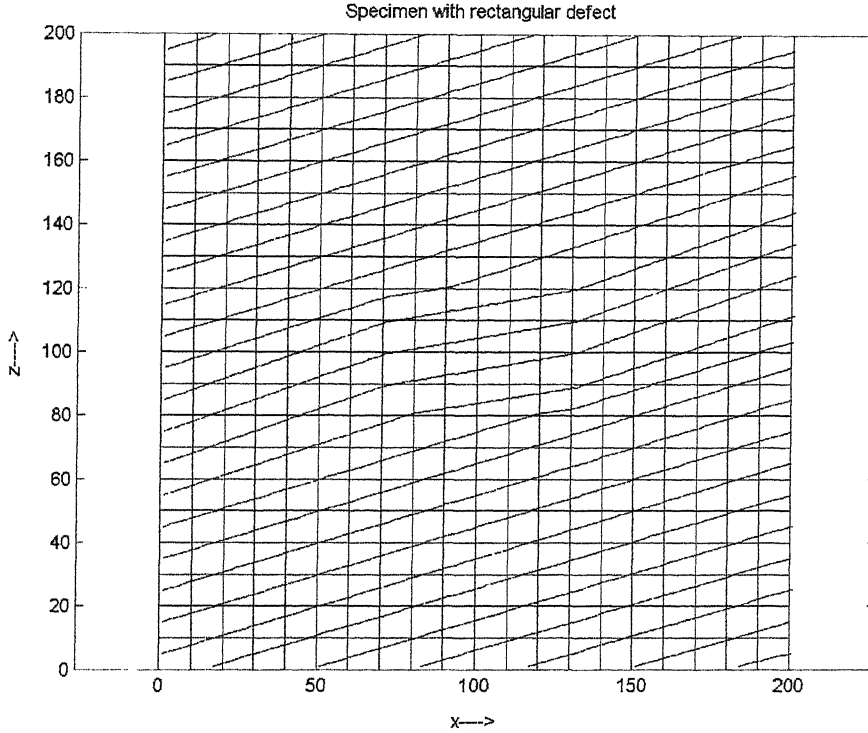


Figure 5.1 Ray paths for group velocity angle 16.7 degree

Graphite/Epoxy with material properties  $C_{11}=145$  GPa,  $C_{12}=10.20$  GPa,  $C_{22}=C_{33}=13.50$  GPa,  $C_{44}=3.40$  GPa,  $C_{66}=6.80$  GPa, density =  $1600 \text{ kg/m}^3$  and fibers are oriented along x-axis. The size of the defect is  $6 \times 4$  mm and defect properties are taken to be  $C_{11}=220$  GPa,  $C_{12}=10.20$  GPa,  $C_{22}=C_{33}=7.0$  GPa,  $C_{44}=3.40$  GPa,  $C_{66}=6.80$  GPa, density =  $2500 \text{ kg/m}^3$  and fibers are oriented along x-axis. Initial guess is taken as  $C_{11}=120$  GPa,  $C_{12}=10.20$  GPa,  $C_{22}=C_{33}=10$  GPa,  $C_{44}=3.40$  GPa,  $C_{66}=6.80$  GPa, density =  $1500 \text{ kg/m}^3$ . Parameters to be reconstructed are  $C_{11}$ ,  $C_{33}$  and density. Rectangular defect used for simulation is shown in figure 5.1 and 5.2. View angles used for simulation are  $0^\circ$ ,  $90^\circ$ ,  $16.7^\circ$  and  $73.3^\circ$ . Initially it was desired to take view angles as  $0^\circ$ ,  $90^\circ$ ,  $15^\circ$  and  $75^\circ$ , but to receive rays at the center of pixel on the specimen boundary; the view angles are slightly modified. The number of projections on a pixel is more than parameters considered.

Figure 5.3-5.5 shows final reconstructed image after 5 iterations. The average error, after each iteration is shown in figure 5.6. Average error is calculated as

$$\text{Average error} = \frac{1}{N} \sum_{i=1}^N \frac{|f_i^{\text{estimated}} - f_i^{\text{actual}}|}{f_i^{\text{actual}}} \times 100 \quad (5.1)$$

where  $N$ =total number of pixels,

$f_i^{estimated}$  = calculated material property for  $i^{th}$  pixel after the iteration

$f_i^{actual}$  = actual material property for  $i^{th}$  pixel

The maximum error for  $C_{11}$ ,  $C_{33}$  and density are 24.14 percent, 65.8 percent and 14.6 percent respectively. The maximum error in  $C_{33}$  is very high, as some of the defect pixels are not identified clearly. The defect is approximately identified by above images. From reconstructed images it can be observed that a ray passing through the defect influences the pixels of parent material, present in its ray path. Also, the convergence is observed much faster in parent material than defect material. Effect of view angles on reconstructed image can be observed easily. It can be seen that average error decreases with successive iterations. Density shows a faster convergence as compared to other elastic constants.

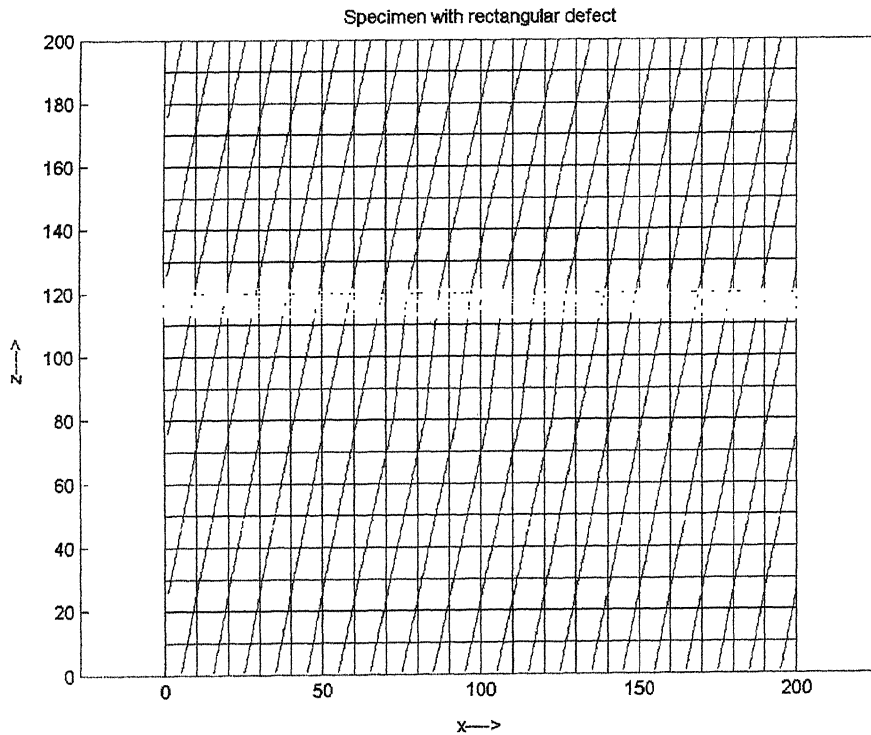


Figure 5.2 Ray paths for group velocity angle  $73.3^\circ$



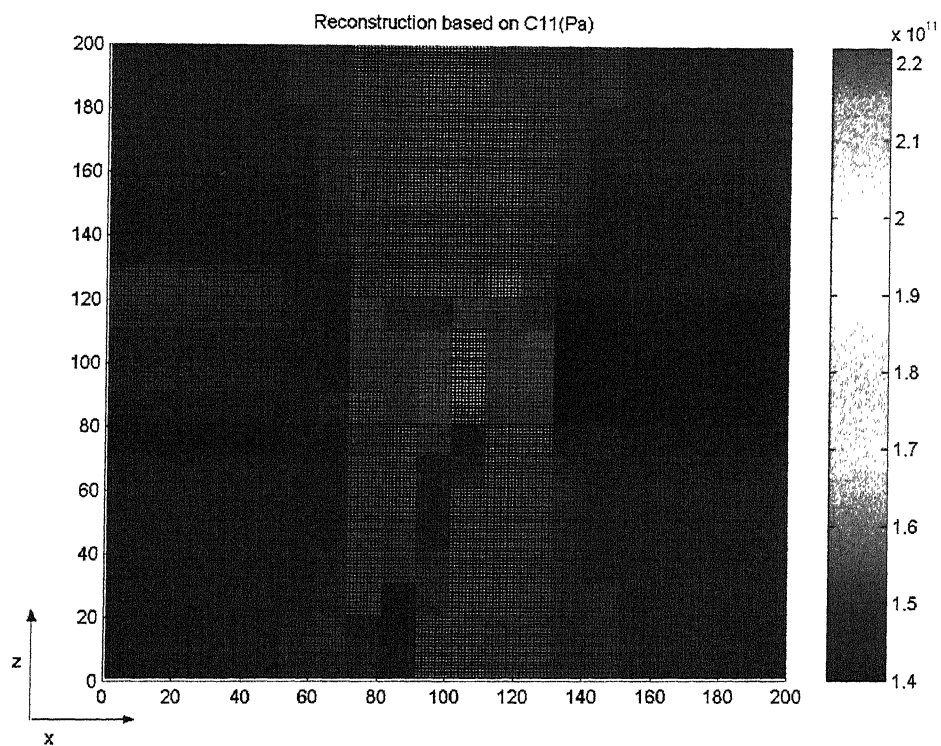


Figure 5.3 Reconstruction based on  $C_{11}$  for rectangular defect

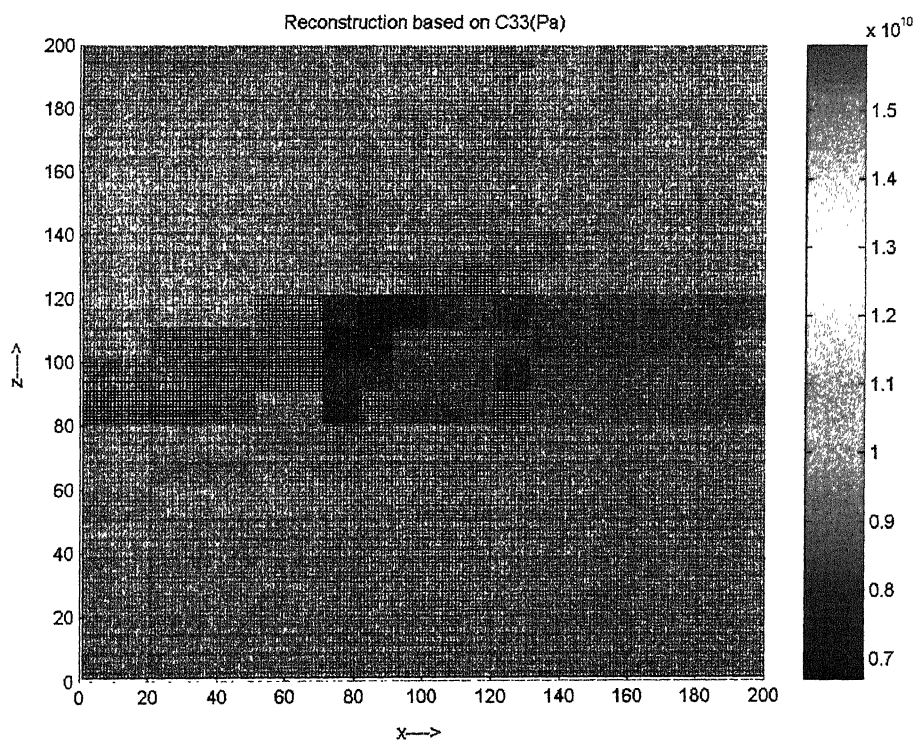


Figure 5.4 Reconstruction based on  $C_{33}$  for rectangular defect

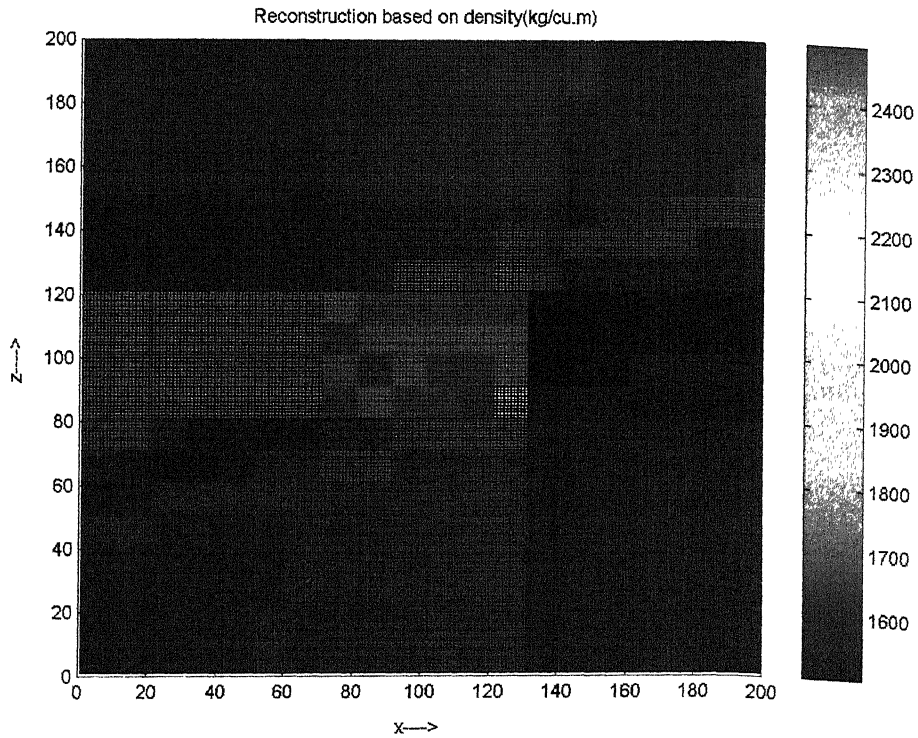


Figure 5.5 Reconstructed based on density for rectangular defect

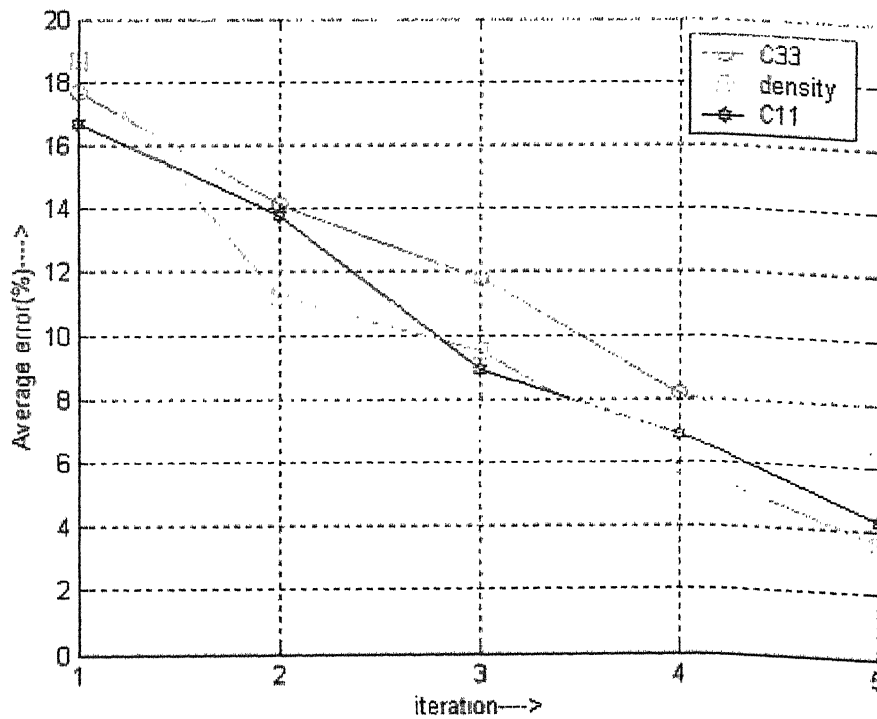


Figure 5.6 Variation of average error with iteration

### 5.1.2 Elliptical defect

Tomographic reconstruction is applied to the specimen with elliptical defect (figure 5.7). The size of the specimen is 20×20 mm. The x-axis and y-axis represents pixel number, from origin, along x-axis and z-axis respectively. The center of the ellipse is at (10,12) with major radius of 5 mm and minor radius of 3 mm. The parent material is Austenite with material properties  $C_{11}=220$  GPa,  $C_{12}=145$  GPa,  $C_{22}=C_{33}=150$  GPa,  $C_{44}=129$  GPa,  $C_{66}=129$  GPa, density = 8100 kg/m<sup>3</sup> and grain orientation is along x-axis. Defect properties are taken as  $C_{11}=80$  GPa,  $C_{12}=145$  GPa,  $C_{22}=C_{33}=70$  GPa,  $C_{44}=129$  GPa,  $C_{66}=129$  GPa, density = 6500 kg/m<sup>3</sup>, grain orientation along x-axis. Initial guess is taken as  $C_{11}=175$  GPa,  $C_{12}=145$  GPa,  $C_{22}=C_{33}=110$  GPa,  $C_{44}=129$  GPa,  $C_{66}=129$  GPa, density = 7500 kg/m<sup>3</sup> and grain orientation along x-axis. Parameters to be reconstructed are  $C_{11}$ ,  $C_{33}$  and density. It is proposed to have view angles of 15°, 75°, 105° and 165° but to make the rays reach at the center of pixels the actual angles are taken to be 16.7°, 73.3°, 163.3° and 106.7°. Figure 5.8 shows ray path for view angle 73.3°, used for simulation. Edge detection is applied after three iterations. Effect of edge detection can be observed in Figure 5.8.

The final reconstructed images for  $C_{11}$ ,  $C_{33}$  and density are shown in figure 5.9, 5.10 and 5.11 respectively. Figure 5.13 shows the average error for all these properties. It can be observed that, in this case, density converges faster as compared to other properties. Figure 5.12 shows the reconstruction of  $C_{11}$  at various stages. The shape of the figure can be identified in 2<sup>nd</sup> iteration itself but the error in  $C_{11}$  is high and a drop in error from 1<sup>st</sup> iteration to 6<sup>th</sup> iteration can be observed. After 6<sup>th</sup> iteration the  $C_{11}$  values for parent as well as defect pixels converge to actual values. Effect of view angles can be figured out from these reconstructed images. It can be observed that, after 3<sup>rd</sup> iteration, application of edge detection, results into faster convergence.

The maximum errors, after 6<sup>th</sup> iteration, for  $C_{11}$ ,  $C_{33}$  and density are 27.3 percent, 39.8 percent and 24.61 percent respectively. Error in  $C_{33}$  is high, as some defect pixels are not identified exactly.

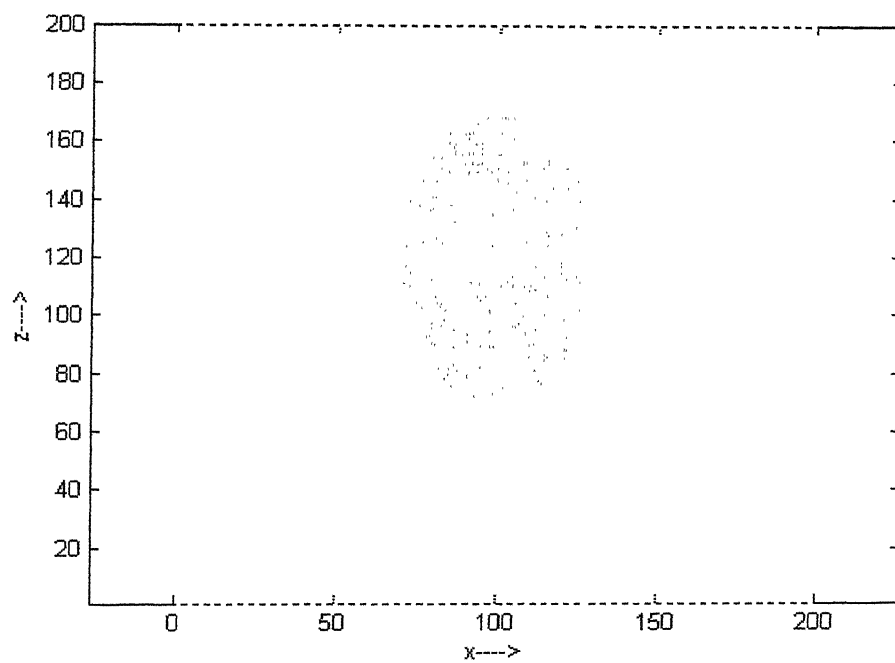


Figure 5.7 Specimen with elliptical defect.

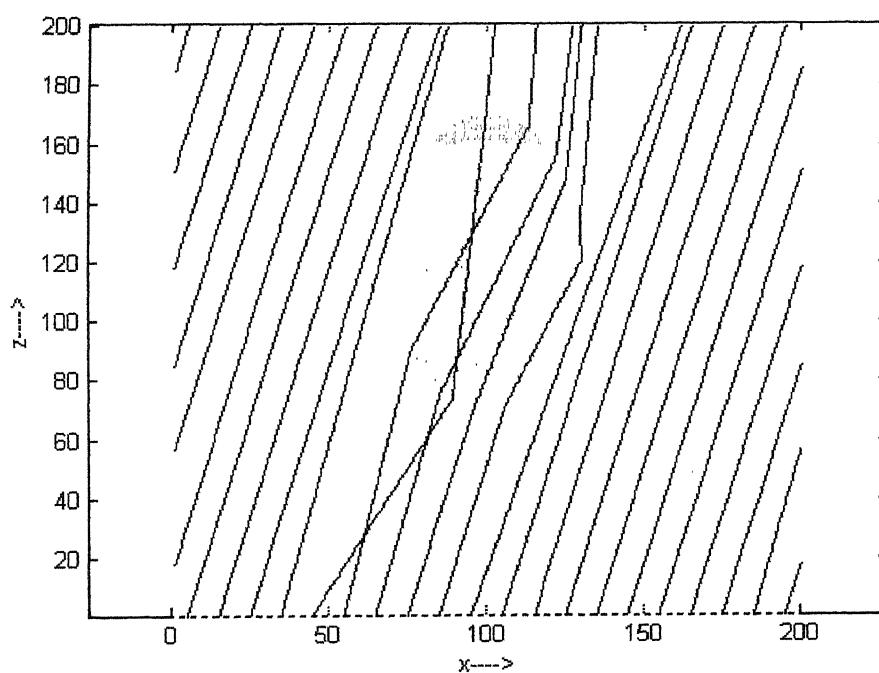


Figure 5.8 Ray path for group velocity angle  $73.3^\circ$

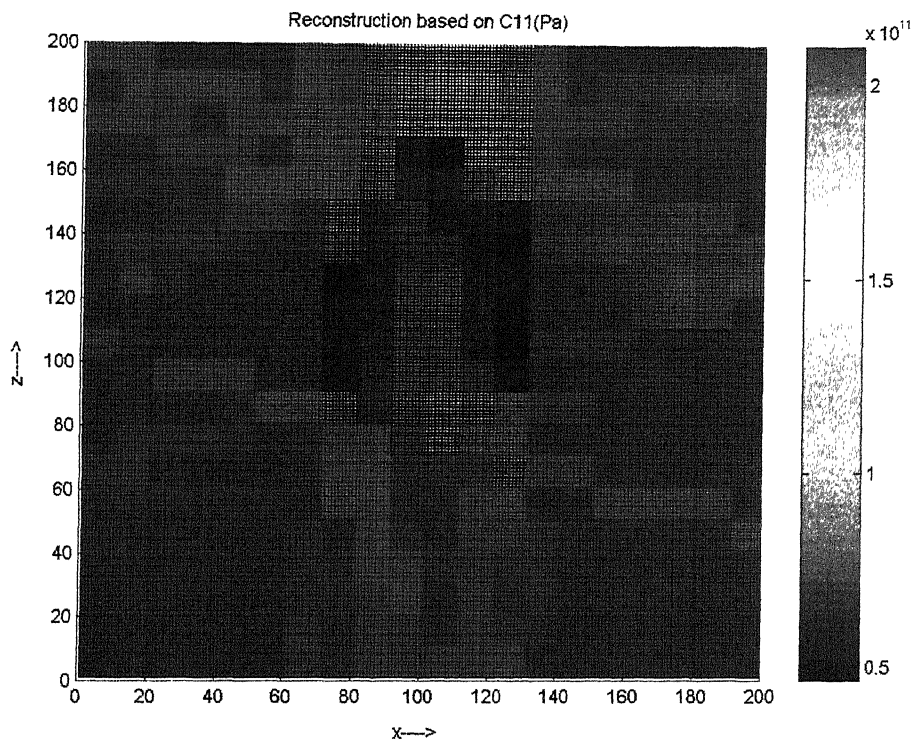


Figure 5.9 Reconstruction based on  $C_{11}$  for elliptical defect.

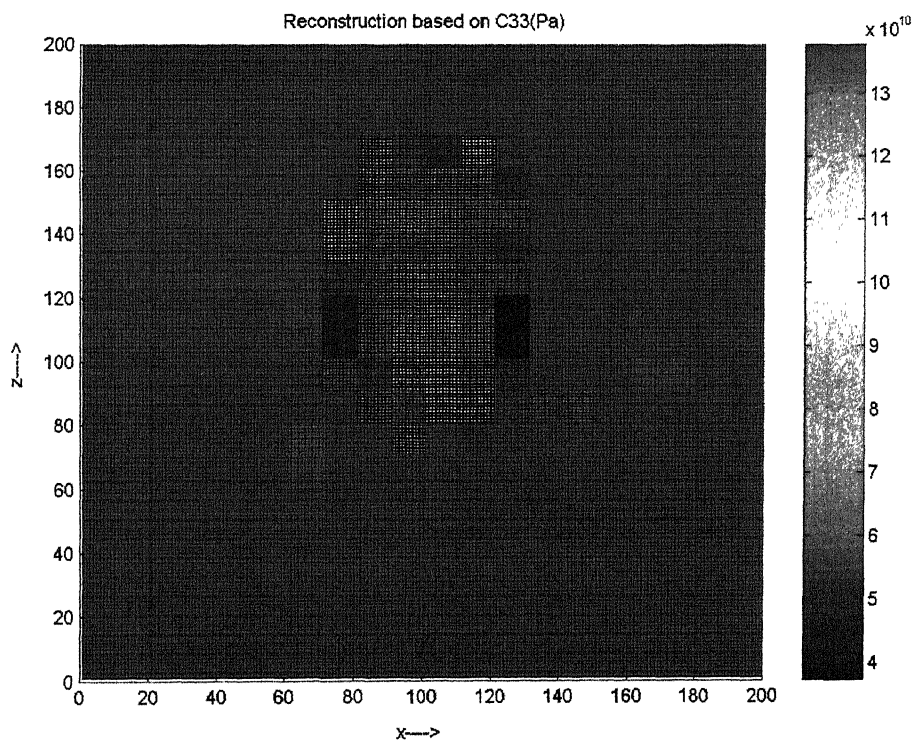


Figure 5.10 Reconstruction based on  $C_{33}$  for elliptical defect.

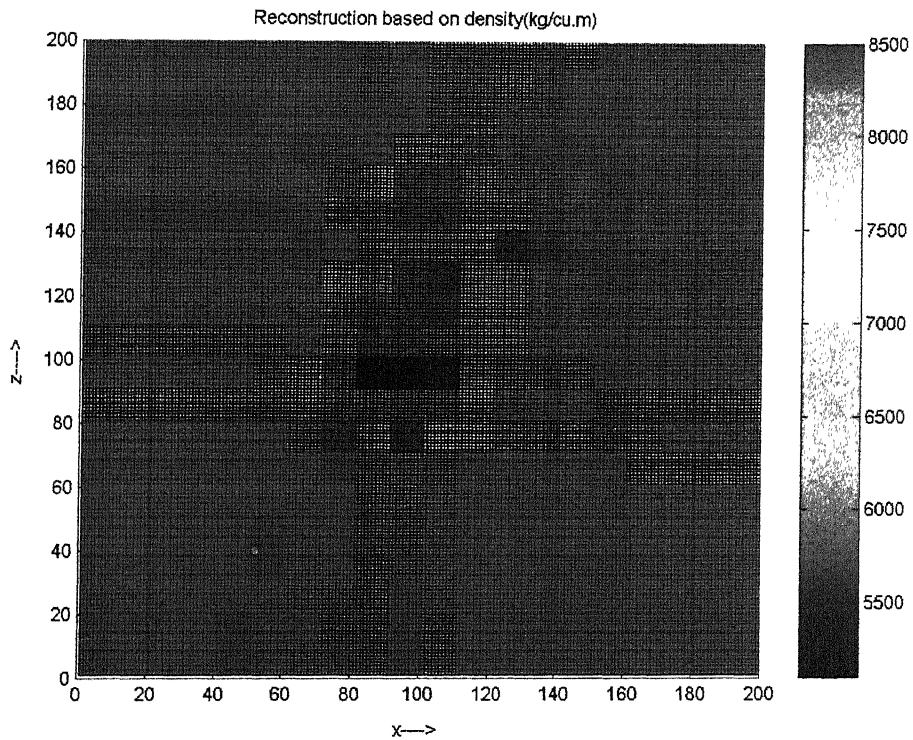


Figure 5.11 Reconstruction based on density for elliptical defect

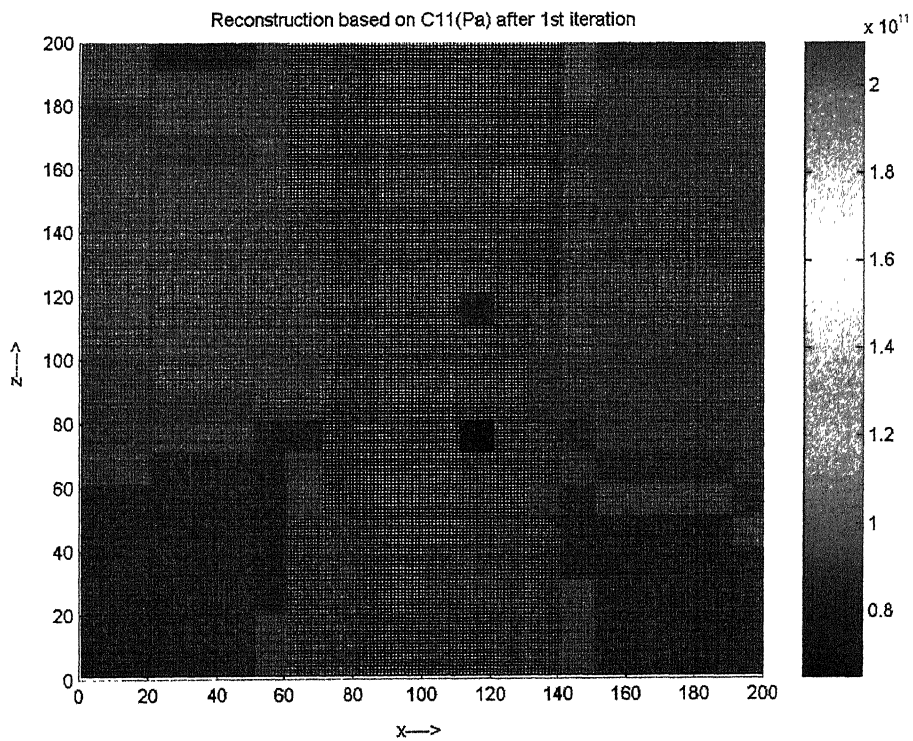


Figure 5.12(a) Reconstruction based on  $C_{11}$  after 1<sup>st</sup> iteration for elliptical defect



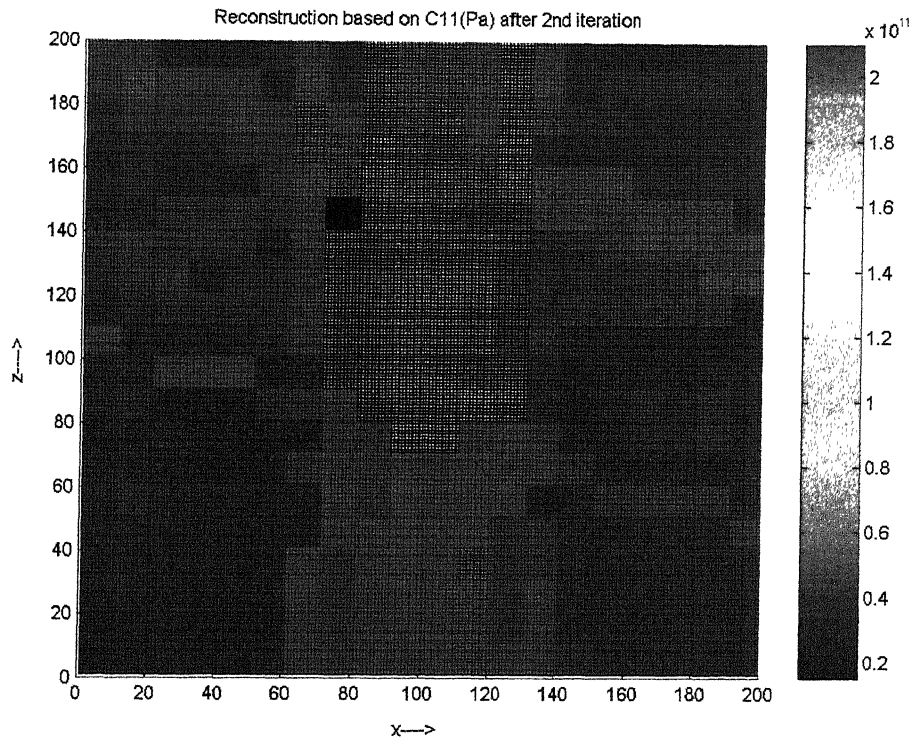


Figure 5.12(b) Reconstruction based on  $C_{11}$  after 2<sup>nd</sup> iteration for elliptical defect

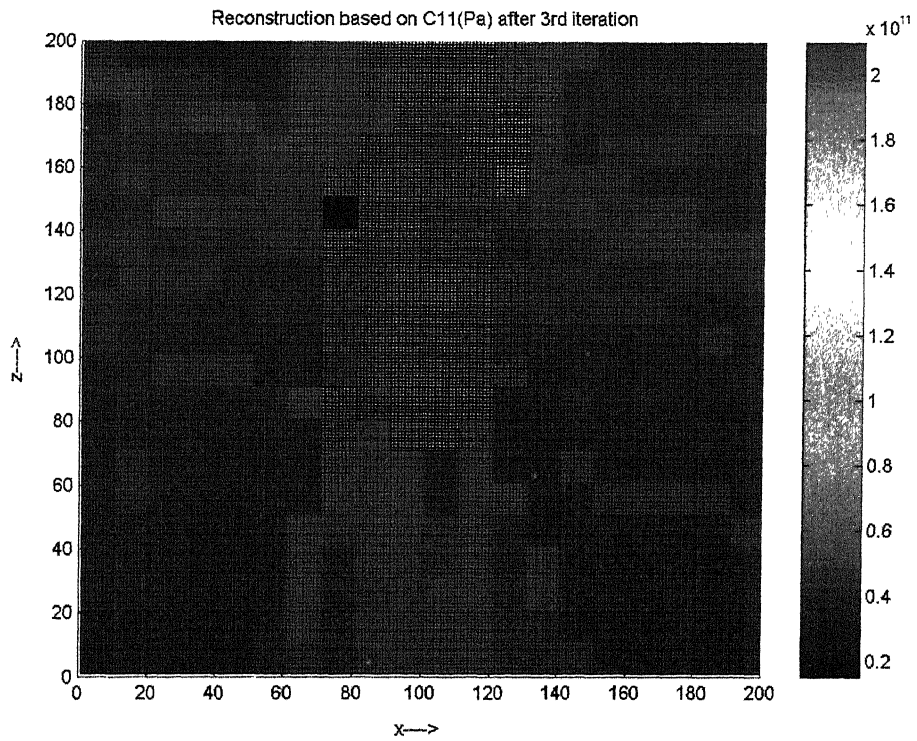


Figure 5.12(c) Reconstruction based on  $C_{11}$  after 3<sup>rd</sup> iteration for elliptical defect

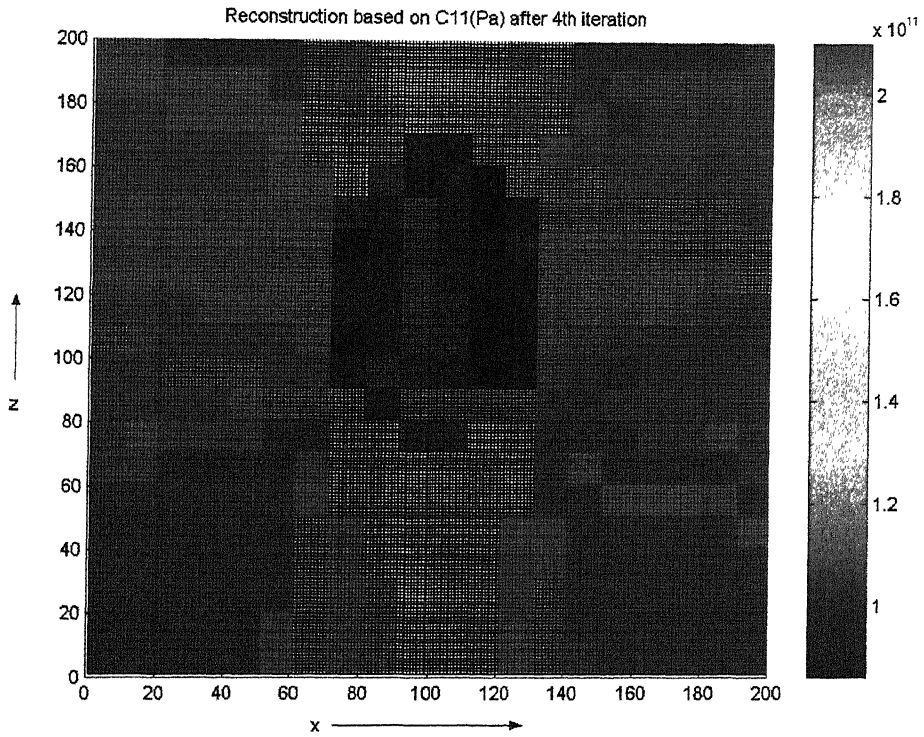


Figure 5.12(d) Reconstruction based on  $C_{11}$  after 4<sup>th</sup> iteration for elliptical defect

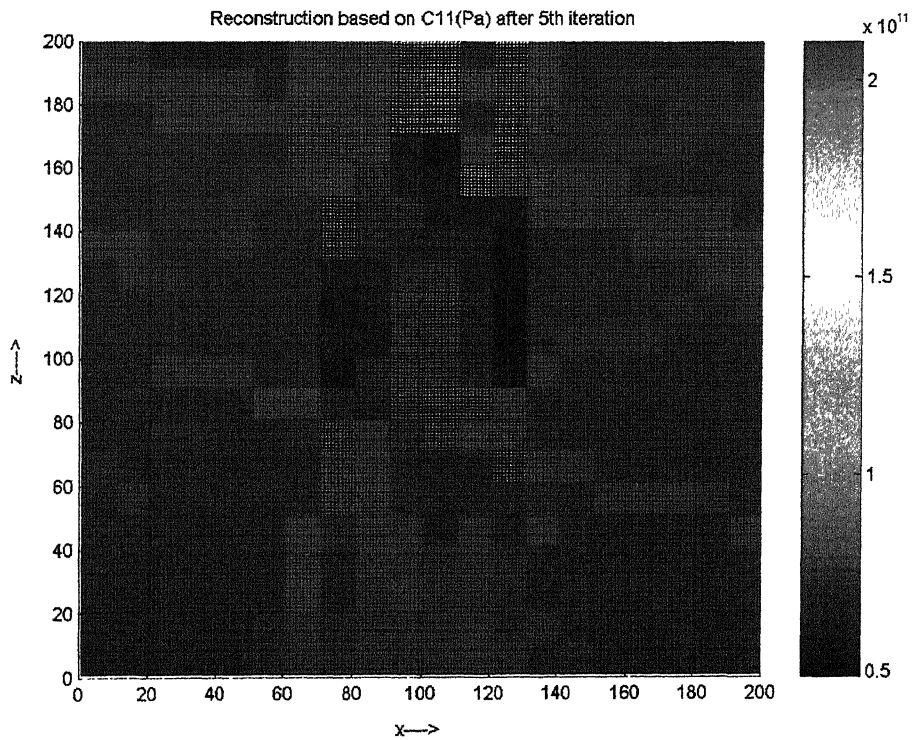


Figure 5.12(e) Reconstruction based on  $C_{11}$  after 5<sup>th</sup> iteration for elliptical defect



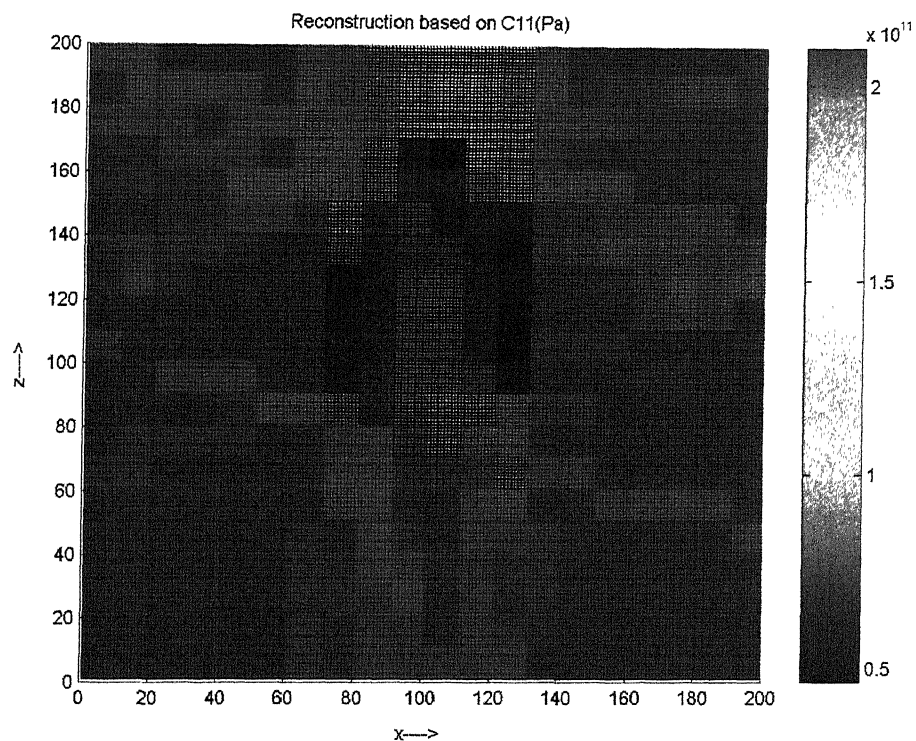


Figure 5.12(f) Reconstruction based on  $C_{11}$  after 6<sup>th</sup> iteration for elliptical defect

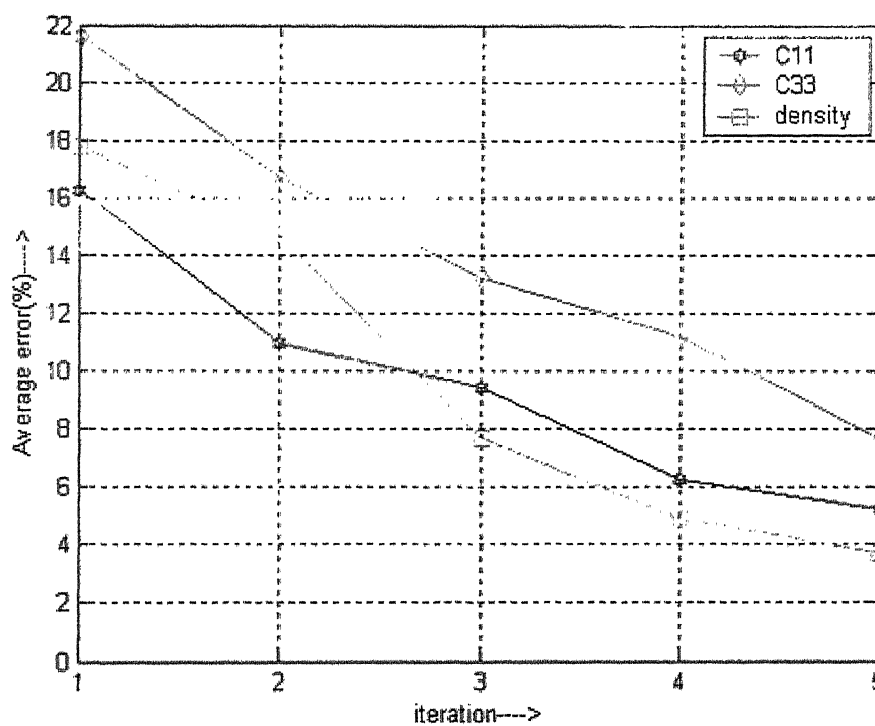


Figure 5.13 Variation of average error with iteration

## 5.2 RECONSTRUCTION USING EXPERIMENTAL DATA

The performance of the proposed tomographic algorithms in the context of experimental data is reported in the present section. An experimental set up has been developed in the laboratory by Mr. Gola Dalliraju and Mr Sarin, whose details are given in appendix B. The specimen size is 30×30 mm, with square defect of size 10×10 mm in center (Figure 5.14). The parent material is glass/epoxy and the defect is of Aluminum. For the considered specimen, volume fraction for the glass fiber is 0.45 (determined by Burn testing performed by Yekambar Rao, in Fracture Mechanics Lab). For the volume fraction 0.45, the material properties for Glass/epoxy are found to be  $C_{11}=39.17$  GPa,  $C_{33}=8.4$  GPa,  $C_{13}=2.18$  GPa,  $C_{66}=4.14$  GPa and density =1800 kg/m<sup>3</sup>. For defect, grain orientation is considered along y-axis. The experimental data is used for image reconstruction based on  $C_{11}$  only. The view angles, 0° and 90° are used for experiments. Initial guess considered for reconstruction is  $C_{11}=35$  GPa. Experimental data used for reconstruction is included in Appendix B.

For tomographic reconstruction time of flight data is determined for both view angles. The reconstructed image after 8 iterations is shown in figure 5.15. Average error for defect, considering actual values as,  $C_{11}=72.5$  GPa is determined. Average error in determination of  $C_{11}$  is found to be 12.14 percent. After 8 iterations, the average value of  $C_{11}$  for parent and defect material is found to be 44.6 GPa and 63.7 GPa respectively.

Reconstructed images for experimental data showed similar kind of convergence as shown by simulation. However the error involved in image reconstructed from experimental data is higher. Errors in experimental data can be associated with misalignment of the laser beam and the inaccuracy in image processing operations. The reconstruction quality obtained from experimental data is satisfactory. The top-right edge of defect is not detected properly by the algorithm, due to presence of noise in experimental data. Reconstruction image for  $C_{11}$  (Figure 5.15) shows that effect of rays at 0° is dominating. Pixels present in right side of defect do not show proper convergence for reconstruction of parameter  $C_{11}$  due to noise in experimental data.

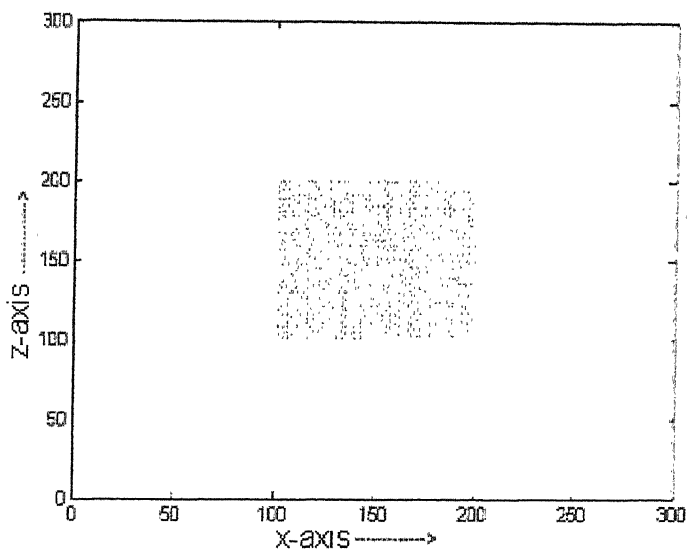


Figure 5.14 Specimen with square defect

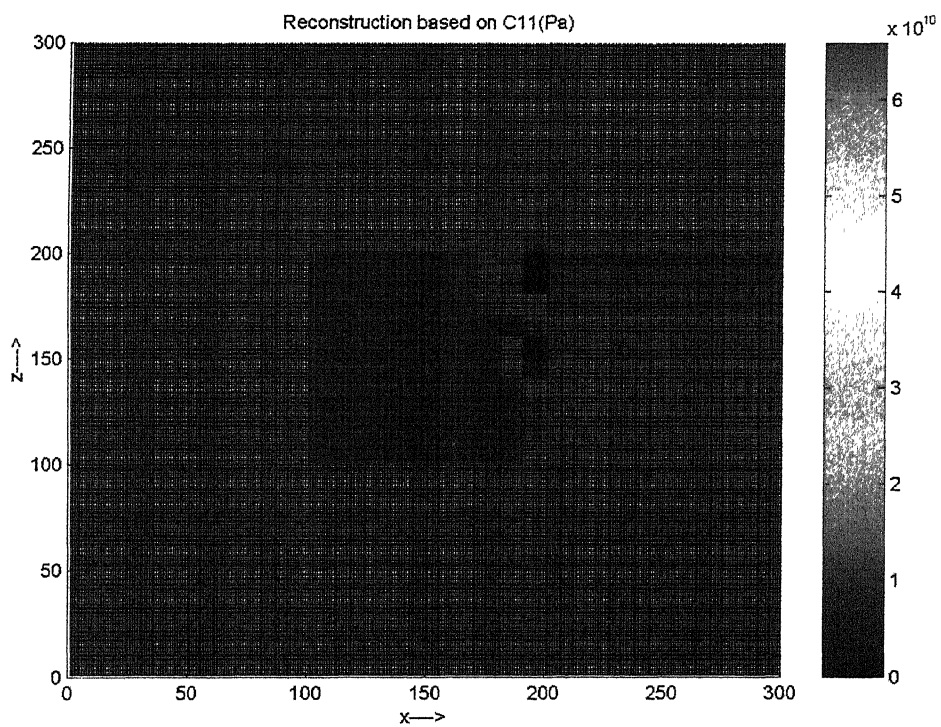


Figure 5.15 Image reconstruction for  $C_{11}$  using experimental data.

### 5.3 EFFECT OF VARIOUS PARAMETERS ON THE PERFORMANCE OF ALGORITHM

In this section, performance of the algorithm as a function of different parameters is studied.

- **Effect of initial guess**

Initial guess of the elastic constants have a significant effect on the convergence of the parameters (table 5.1). Convergence is poor if difference in initial guess and actual value is high as shown below.

Table 5.1 Effect of initial guess on average error (after 5 iterations)

Initial guess/actual value (%)	10	50	80	90	110	150
Average Error (%)	28.2	16.7	4.7	2.5	3.1	15.9

- **Effect of relaxation parameter**

The relaxation parameter influences the rate of convergence. Figure 5.16 shows average error observed for different relaxation parameter. There is no significant difference in the quality of results for all values except at very low value. The value of relaxation parameter recommended is between 0.8 and 1.2.

- **Effect of number of Projections**

As the number of projections through a pixel is taken more than parameters for reconstruction, a faster convergence is observed. Figure 5.17 shows how average error reduces when the number of projections taken in a pixel is increased. It can be observed that rate of convergence is faster for more number of projections but after certain limit, no significant improvement could be observed. Generally, for  $n$  parameters,  $2n$  projections through a pixel give optimum results.

- **Effect of edge detection**

On application of edge detection results show better convergence. Figure 5.18 and 5.19 shows reconstructed images for  $C_{11}$  without applying and applying edge detection. The average error without considering edge detection is 8.6 percent, after

5<sup>th</sup> iteration. While on applying edge detection, the average error reduced to 3.8 percent.

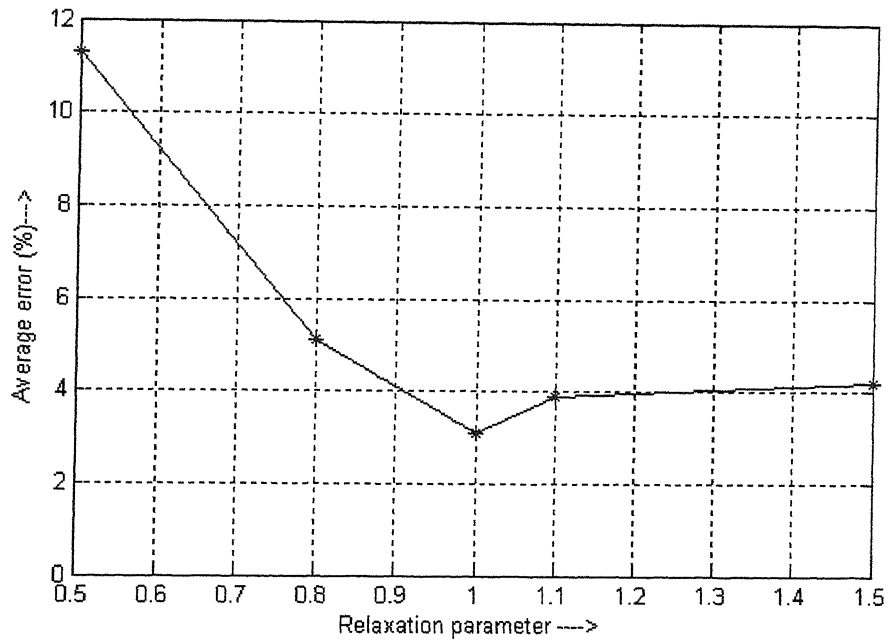


Figure5.16 Average error vs. relaxation parameter.

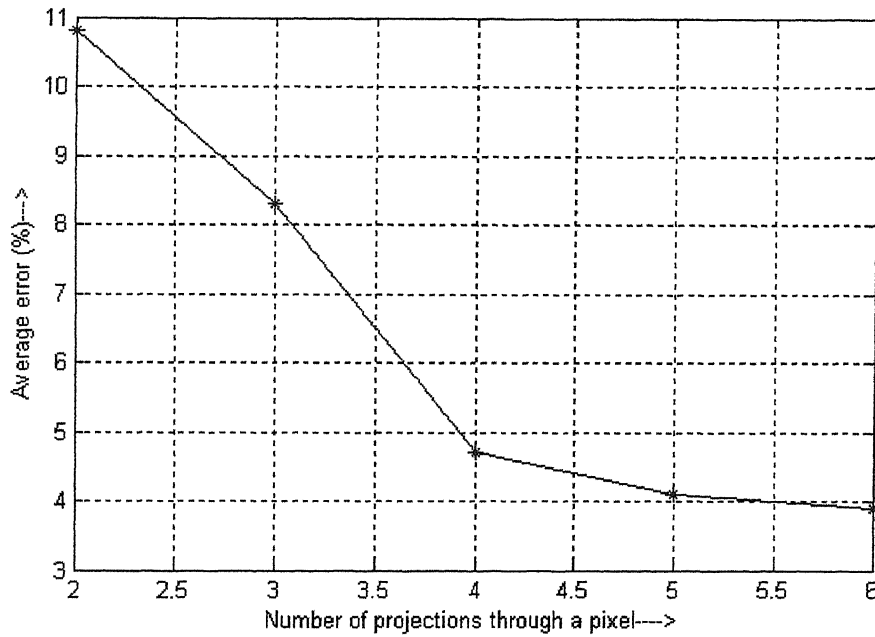


Figure 5.17 Effect of Number of projections through a pixel on performance of the algorithm

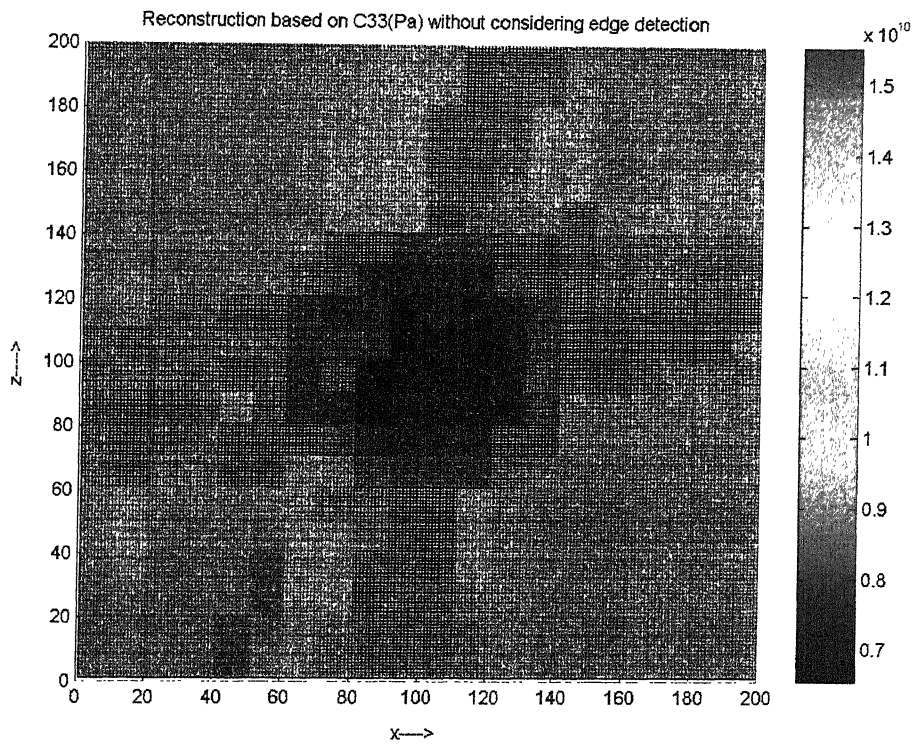


Figure 5.18 Reconstructed image for  $C_{33}$  without applying edge detection.

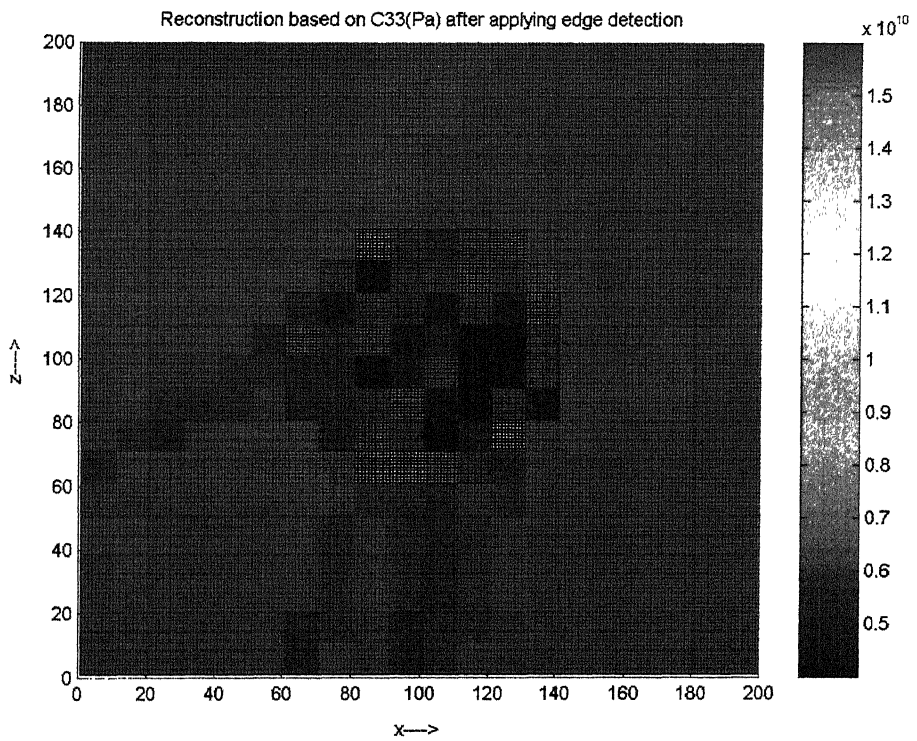


Figure 5.19 Reconstructed image for  $C_{33}$  after applying edge detection.

## **5.4 CLOSURE**

In this chapter, present model is applied on simulated and experimental data and results are summarized. Effect of various parameters on the performance of reconstruction algorithm is discussed.

## Chapter 6

# Conclusions and Scope for Future work

### 6.1 CONCLUSIONS

A tomographic image reconstruction model, applying ray tracing, has been developed. It is applied to determine principal elastic constants and density of composite materials. The model is very useful to predict and understand the effects of various parameters on tomographic image reconstruction. From this study, following conclusions can be drawn.

- The performance of tomographic image reconstruction model is improved when number of projections considered from a pixel is much more than number of parameters considered for optimization.
- Application of edge detection on the ray tracing algorithm, improves the resolution of reconstructed image and average error is reduced.
- It has been found that if a specimen is scanned across a surface at constant beam angle, then there is a possibility that ultrasonic ray energy may not penetrate certain regions. Therefore in such cases to ensure that the whole component can be examined, more than one probe angle may be needed.
- Application of ray tracing in tomographic reconstruction, insures a good rate of convergence. The model is found to be successful in the reconstruction of images and determination of material properties, for rectangular as well as curved defects.

### 6.2 SCOPE FOR FUTURE WORK

- The method can be extended for determination of shear modulus, rigidity modulus and fiber orientation of composite materials.
- The model can be extended for a combination of quasi-longitudinal and quasi-shear waves for identification of defects.
- With few modifications, triangular pixels can be taken, instead rectangular. This will improve the accuracy when defects are in curved shape.



## References

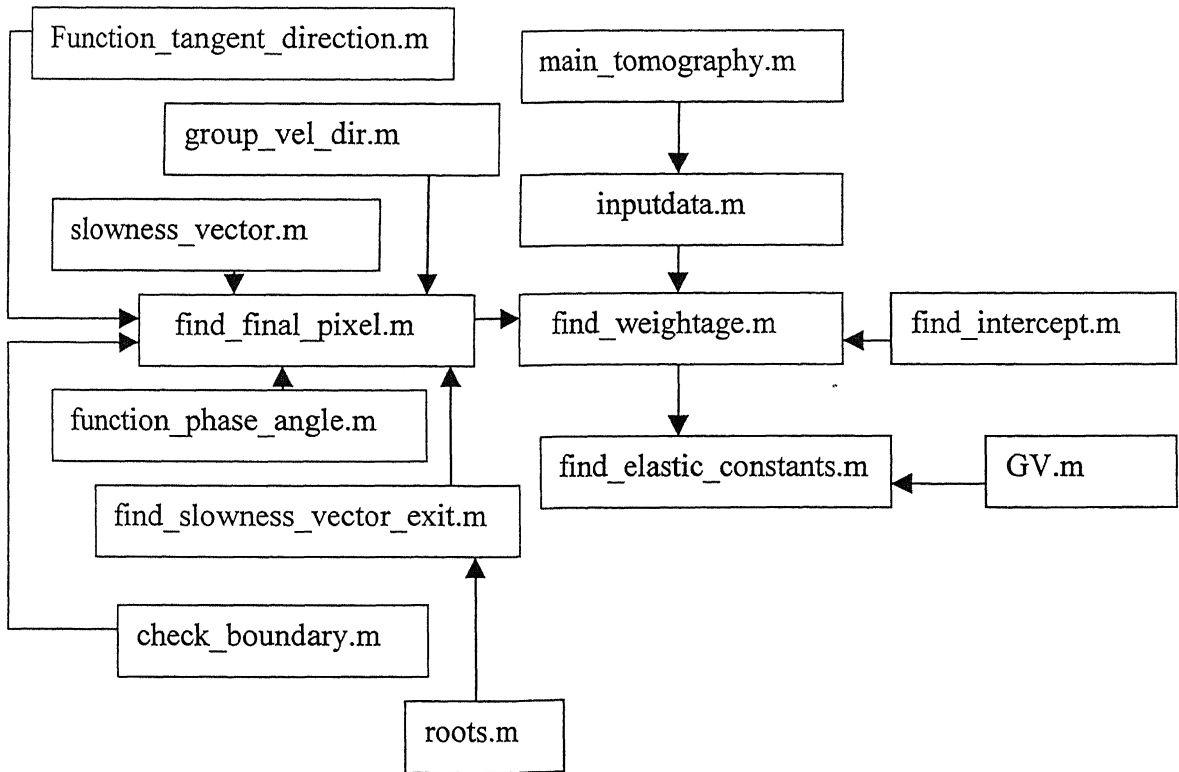
1. Synge, J. L., "Elastic waves in anisotropic media", *J. Math. and Phys.*, Vol.35, 1957, pp 323-334
2. Musgrave M.J.P., "Crystal Acoustics", Holden Day, 1970
3. Silk, "A computer model for ultrasonic propagation in complex orthotropic structure", *Ultrasonics*, Vol. 19, 1981, pp 208-212.
4. Ogilvy J.A., "A model for ultrasonic inspection of composite plates", *Ultrasonics* Vol. 33, No. 2, 1995, pp 85-93
5. Rokhlin S.I., Bolland T.K., Adler L., "Reflection and Refraction of elastic waves on a plane interface between two generally anisotropic media", *Journal of Acoustical society of America*, Vol. 79, No. 4, April 1986, pp 210-217.
6. Ogilvy J.A., "The influence of Austenitic weld geometry and manufacture on ultrasonic inspection of welded joints", *British Journal of NDT*, Vol.29, 1987, pp 147-155
7. Ogilvy J.A., "Computerized ultrasonic ray tracing in austenitic steel", *NDT International*, Vol. 18, No. 2, April 1985, pp 67-77.
8. Ogilvy J.A., "An iterative ray tracing model for ultrasonic nondestructive testing", *NDT & E International*, Vol. 25, 1992, pp 3-9.
9. Schmitz V., Walte F., Chaklov S.V., "3D ray tracing in austenite materials", *NDT & E International*, Vol. 32, 1999, pp 201-213.
10. Thomsen Leon, "Weak elastic anisotropy", *Geophysics*, Vol. 15(10), 1986, pp 1954-1966.
11. Stewart R.R., "An algebraic reconstruction technique for weakly anisotropic velocity." *Geophysics*, 53(12), 1988, pp 1613-1615.
12. Jansen D.P., Chow T., Hutchins D. A., Young R.P., "Ultrasonic tomographic imaging of anisotropic media.", *acoustical Imaging*, Vol.19, 1992, pp 59-63..
13. Chow T.M., Hutchins D.A., Mottram J.T., "Simultaneous acoustic emission and ultrasonic tomographic imaging in anisotropic polymer composite materials." *Journal of Acoustical society of America*, Vol.94, No.2, 1993, pp 944-953.

14. Kline R. A., Wang Y. Q., "A technique for ultrasonic tomography in anisotropic media." *Journal of Acoustical society of America*, Vol. 91, No. 2, 1992, pp 878-884.
15. Wang Y Q., Kline R A., "A new technique for multiparameter image reconstruction using a tomographic approach." *Rev. Prog. QNDE*, Vol.13, 1994, pp 943-950.
16. Braun Hans, Hauck Axel, "Tomographic reconstruction of vector fields.", *IEEE trans on signal processing*, Vol. 39(2), 1991, pp 464-471.
17. Fedorov F. I., "Theory of elastic waves in crystals.", Plenum Press.
18. Chen H.C, "Theory of Electromagnetic Waves-A coordinate free approach", (McGraw-Hill, New York, 1983).
19. N.N.Kishore, D.Datta, "Trends in NDE Science & Technology", *Proceedings of the 14th World Conference on Non-Destructive Testing*, New Delhi, 8-13 December 1996. Vol. 4, pages 2139 - 2144.
20. Herman G.T., "Image Reconstruction from Projections." Academic Press, New York, 1980
21. D. Mishra, K. Murlidhar, P. Munshi, "A robust MART algorithm for Tomographic calculations", *Numerical Heat Transfer, Part B*, Vol 35, 1999, pp 485-506.

This Appendix will describe the file structure of the program developed in the present work and it will discuss different functions used in the program.

### File structure

In whole 16 function files are used in the program. Each function file performs one or more specific tasks. The basic structure of the whole program based on these files is given in the form of flowchart below.



### Functions used in the program

`main_tomography.m` : It is the main program. Different functions are called in it and it determines the elastic constants for each pixel after each iteration and updates the pixel properties.

inputdata.m : It specifies the specimen geometry, no. of pixels, initial guess for elastic constants. Time of flight data including Scanner position, Receiver position are also specified in it. In addition, it specifies step size for ray tracing.

find\_weightage.m : for a given Scanner position and Receiver position, it determines the ray which is reaching to receiver position through an iterative procedure. Then it calls function find\_intercept.m to calculate the intercept in each pixel for the ray.

find\_final\_pixel.m : It determines the final pixel of a ray, for given Scanner position and group velocity angle. It stores the ray path and pixel properties for each pixel in the ray.

check\_boundary.m : It checks if ray has reached the specimen boundary or not.

function\_phase\_angle: For given material properties and group velocity angle it determines the phase angle.

function\_tangent\_direction.m : For given interface pixel, it approximates a curve and find the tangent and normal direction at the interface.

slowness\_vector.m: It calculates the slowness vector for given material properties, group velocity angle and phase angle.

slowness\_vector\_exit.m: It calculates the slowness vector, when ray reaches an interface, and refracts according to change in material properties.

find\_intercept.m : For a given ray path, it determines the intercept length for each pixel, and calculates the corrected group velocity using ART algorithm. It stores the information required for elastic constant determination for each pixel.

group\_vel\_direction.m: It calculates the group velocity direction for given phase angle and material properties.

roots.m : It calculates the roots of 4 degree equation required for finding the slowness vector at interface.

find\_elastic\_constants.m : For a given cell, it determines the corrected elastic constants from the corrected group velocity data. It uses Least square nonlinear Matlab inbuilt function to solve for elastic constants.

GV.m : It calculates the error in corrected group velocity and present group velocity and supplies it to find\_elastic\_constant.m.

error\_estimation.m: It calculates the percentage average error in elastic constants at respective pixel ,after each iteration .

tomography.m It calculates the time of flight data for given Scanner position and Receiver position ,which is further used as simulated data for image reconstruction.

## Appendix-B

### Experimental Set Up

This Chapter briefly describes the details of laser based ultrasonic setup and data collection.

#### EXPERIMENTAL SETUP: LASER BASED ULTRASONICS

Nd: YAG Pulse Laser is used to generate ultrasonic waves in any media, which is to be inspected. Heterodyne type Laser Interferometer is used to detect the transmitted wave, the signals are then amplified and digitized using a Yokogawa DL1740 digital oscilloscope. The oscilloscope is triggered using a synchronization signal from the pockels cell of the pulsed laser. Recorded waveforms are transferred to a HP Pentium III computer over a USB/Ethernet interface for subsequent storage and analysis which is then captured in a Digital Storage Oscilloscope. The schematic layout of experimental setup is shown in Fig.B.1 and a photograph of the same is shown as Fig. B.2. Small part of the beam is allowed to fall on the specimen to study the Nd: YAG laser beam characterizations. For this purpose the Teflon material with different slits viz. rectangular of 10mm x 1mm, circular slits of 11mm, 12mm, 13mm and circumferential slits of 1mm width at the mean radii at 4mm, 5mm, 6mm were used. All these slits are made in 125mm Teflon material. A brief description of the setup is given in the following paragraphs.

#### ③ Nd: YAG Pulsed Laser Ultrasonic Generator

The 5000 DNS series pulsed Nd: YAG laser is built on a modular concept. The optical configuration allows variable setting of the optical parameters. It consists of 3 major components, the laser-head, the power supply and the cooling unit. The heart of the system is the pumping structure, which houses the Nd: YAG rod and the flash lamp. The lasers are built on an electro-optically Q-switched oscillator. This oscillator uses a pockels cell Q-switch to produce pulses of high intensity and short duration (5-7 ns). Q- Switched Lasers are often used as a non-contact ultrasound source in non-

destructive testing of materials. Q-switched lasers typically have nanosecond (ns) pulse durations and generate broadband ultrasound waves, though longer laser pulses, of 100 microseconds or greater, have been used for NDE. A variable reflectivity output coupler allows the extraction of high energy on a single spatial transverse mode. This leads to laser beams of low divergence, and to high conversion efficiencies in the harmonic wavelengths (1064, 532, 355, 266 nm). Different harmonic generators extend the wavelength range to the second, third and fourth harmonics.

The active medium of the laser operates on transitions of triply ionized Neodymium atoms ( $\text{Nd}^{3+}$ ), which take place of another ion (Yttrium) in the host: Yttrium Aluminum Garnet known by the acronym YAG. The laser operates as a 4-level system. The intense broad-spectrum light of the flash lamp populates the upper level. Once in the higher energy level, the Neodymium ions drop to a metastable level, producing a population inversion. The lower level decays by a fast non-radiative process to the ground state. The strongest Neodymium line is 1064 nm.

#### ▪ Optical Heterodyne Laser (He-Ne) Probe

The SH-130 probe is designed to measure transient mechanical displacements of very low amplitude. It is specially devoted to measuring displacements generated by the propagation of an acoustic or ultrasonic wave. The system consists of a compact optical head and an electronic signal-processing unit. The optical head integrates high stability, low power laser source for fast detection with a high spatial resolution.

The electronic signal processor delivers a response proportional to the displacement of the target, with a high bandwidth. The output signal is automatically calibrated to give the absolute value of the measured displacement. The principle of detection (heterodyne interferometry) makes the system insensitive to external vibrations. The compactness of the system allows for a wide range of operating conditions.

#### ▪ Digital Storage Oscilloscope (DSO)

The setup utilizes a Yokogawa DL1740 (four channel, one GSa/sec, 500 MHz) Digital Storage Oscilloscope, having built in Zip drive, Ethernet, USB, GPIB and Serial Ports for communication with external PC's/ systems.

- Computer

The DSO is interfaced to a Pentium III based PC and Data is stored on-line using communication through USB and Ethernet ports.

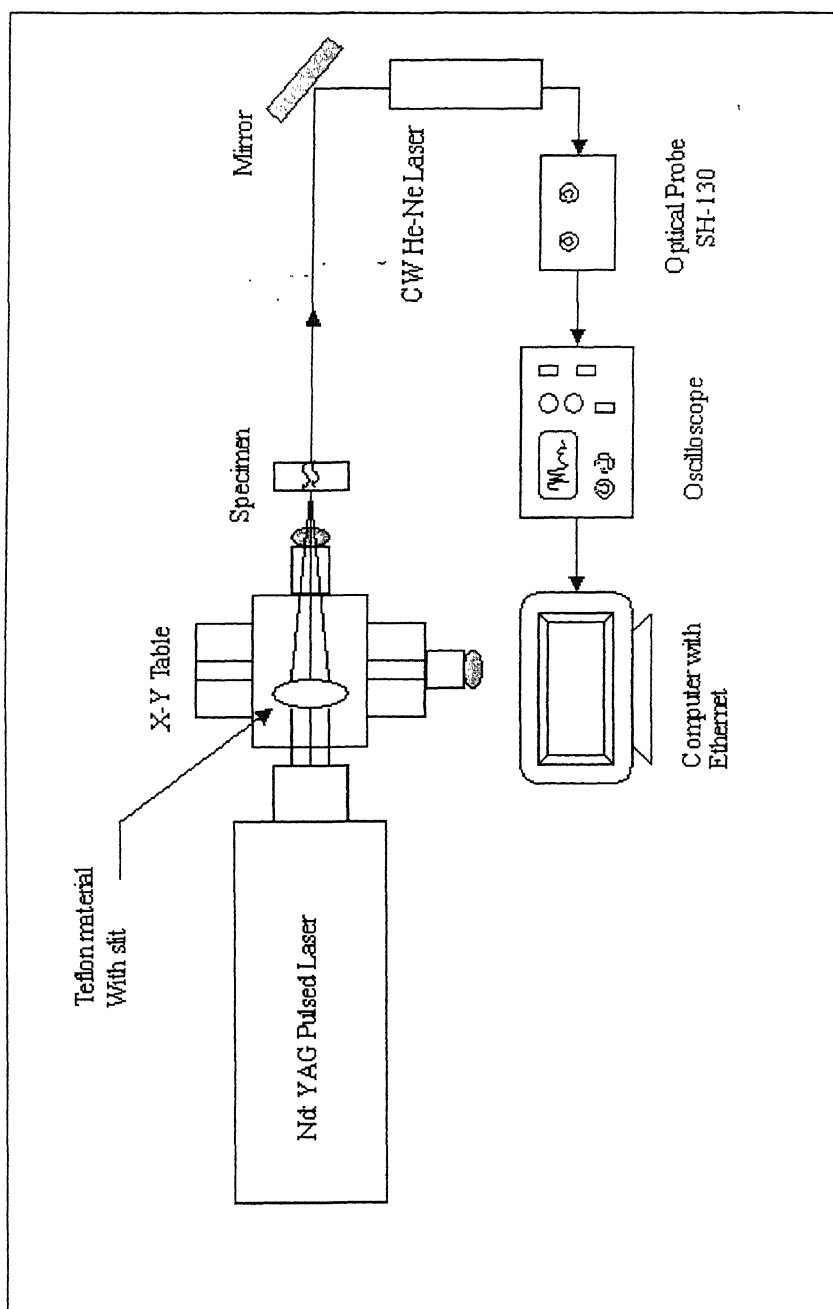


Figure B1 Experimental Set Up



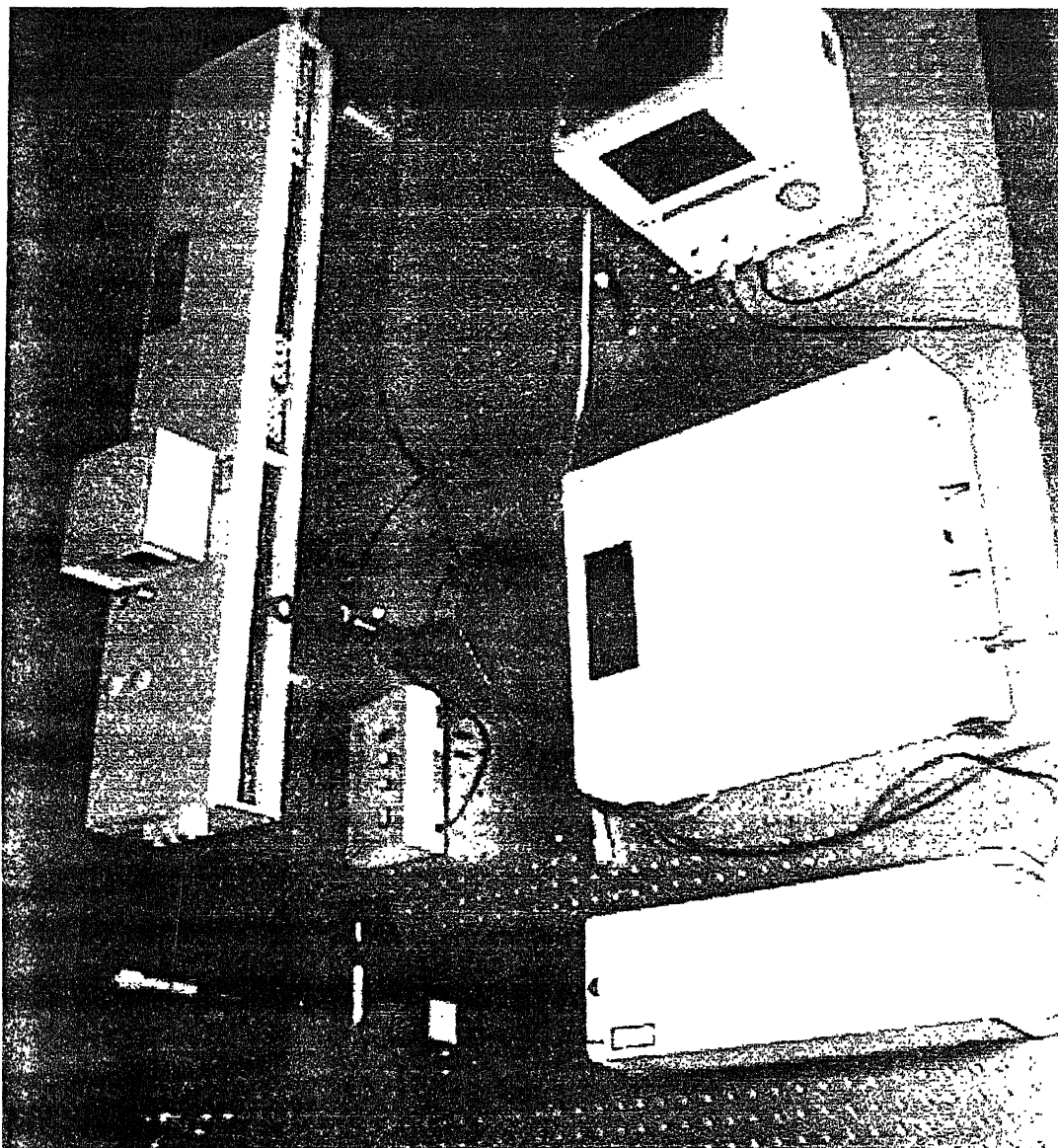


Fig.B.2 Photograph of LBU set-up

## EXPERIMENTAL DATA USED FOR RECONSTRUCTION

x co-ordinate (transmitter)	y co-ordinate (transmitter)	x co-ordinate (receiver)	y co-ordinate (receiver)	time of flight
(mm)	(mm)	(mm)	(mm)	(sec)
0	5	30	5	6.78E-06
0	15	30	15	6.78E-06
0	25	30	25	6.78E-06
0	35	30	35	6.78E-06
0	45	30	45	6.78E-06
0	55	30	55	6.78E-06
0	65	30	65	6.78E-06
0	75	30	75	6.78E-06
0	85	30	85	6.78E-06
0	95	30	95	6.78E-06
0	105	30	105	6.84E-06
0	115	30	115	7.30E-06
0	125	30	125	8.11E-06
0	135	30	135	7.87E-06
0	145	30	145	7.70E-06
0	155	30	155	7.53E-06
0	165	30	165	7.37E-06
0	175	30	175	7.21E-06
0	185	30	185	7.04E-06
0	195	30	195	7.11E-06
0	205	30	205	6.78E-06
0	215	30	215	6.78E-06
0	225	30	225	6.78E-06
0	235	30	235	6.78E-06
0	245	30	245	6.78E-06
0	255	30	255	6.78E-06
0	265	30	265	6.78E-06
0	275	30	275	6.78E-06
0	285	30	285	6.78E-06
0	295	30	295	6.78E-06
5	0	5	30	1.46E-05
15	0	15	30	1.46E-05
25	0	25	30	1.46E-05
35	0	35	30	1.46E-05
45	0	45	30	1.46E-05
55	0	55	30	1.46E-05
65	0	65	30	1.46E-05
75	0	75	30	1.46E-05
85	0	85	30	1.46E-05
95	0	95	30	1.46E-05
105	0	105	30	1.16E-05
115	0	115	30	1.16E-05
125	0	125	30	1.16E-05
135	0	135	30	1.16E-05

x co-ordinate (transmitter)	y co-ordinate (transmitter)	x co-ordinate (receiver)	y co-ordinate (receiver)	time of flight
(mm)	(mm)	(mm)	(mm)	(sec)
145	0	145	30	1.16E-05
155	0	155	30	1.16E-05
165	0	165	30	1.16E-05
175	0	175	30	1.16E-05
185	0	185	30	1.16E-05
195	0	195	30	1.16E-05
205	0	205	30	1.46E-05
215	0	215	30	1.46E-05
225	0	225	30	1.46E-05
235	0	235	30	1.46E-05
245	0	245	30	1.46E-05
255	0	255	30	1.46E-05
265	0	265	30	1.46E-05
275	0	275	30	1.46E-05
285	0	285	30	1.46E-05
295	0	295	30	1.46E-05

A 143463



A143463